INORGANIC CHEMISTRY FRONTIERS

REVIEW

View Article Online
View Journal | View Issue

Cite this: *Inorg. Chem. Front.*, 2023, **10**, 3468

Solvent-free synthetic protocols for halide perovskites

Xinrui Zhang,[a] Jiaomao Zheng,[b] Yifan Wang,[a] Zhenlong Wang,[a] Luyao Zheng,[b] Amin Nozariasbmarz,[b] Kai Tao,[a] Binghe Ma,[a] Bed Poudel,[b] Kai Wang *[b] and Tao Ye*[a]

Received 21st February 2023,
Accepted 2nd May 2023

DOI: 10.1039/d3qi00163f

rsc.li/frontiers-inorganic

Halide perovskites have been extensively researched in the past decade, and explored in fields stepping out from photovoltaics towards photothermal and thermoelectric energy conversion, light-emission, high-energy electromagnetic radiation detection, memristors/artificial synapses, ferroelectricity, *etc.* These frontier applications will fundamentally require a benign material platform of great sample quality but easy accessibility. Traditional synthesis of halide perovskites follows a wet chemistry route, that is, dissolving–precipitation through a solution medium. However, commonly used solvents are of high-cost, environmentally unfriendly, and have high treatment complexity and low post-processing convenience. Breakthroughs on solvent toxicity minimization or even solvent exemption can pave a new roadmap to future development of perovskite-based applications. In this work, we discuss new opportunities in solvent-free synthesis including newly researched vapor deposition and mechanochemical methods, as well as other potential insights in this direction.

Introduction

Halide perovskites have attracted huge attention due to their excellent performance in various optoelectronic fields, including solar energy conversion, light-emission, high energy radiation detection, memristors/artificial synapses, ferroelectrics, photothermal conversion, thermoelectric cooling/energy generation, *etc.* For practical application in any device manifestations, sample quality is of paramount importance to the performance, which is fundamentally correlated to the synthetic methodology.[1] The quality can be defined as features, such as lattice defects, grain size, grain boundary density, surface roughness/coverage/uniformity, topography, and crystalline orientation, of perovskites obtained from different methods, which vary significantly from sample to sample, batch to batch, and so as to the resultant performance at device level. Solution-processing methods have been the dominant synthetic methods for halide perovskite materials, with merits of low-cost, operational ease, and high compatibility for thin film manufacturing, but remaining insufficiently effective in terms of (i) solvent toxicity considerations, (ii) residual solvent induced instability issues, and (iii) timely and energetically effortful synthesis for bulk samples.[2]

Briefly, most typically used solvents (*e.g.*, *N*,*N*-dimethylformamide (DMF), *N*-methyl-2-pyrrolidone (NMP), dimethyl sulfoxide (DMSO), and *N*,*N*-dimethylacetamide (DMAC)) are of high toxicity (both DMF and DMAC are classified as substances of very high concern (SVHCs) and toxic to reproduction by the European Chemicals Agency (ECHA)), requiring additional purification techniques when considering real manufacturing at large scale.[3] Secondly, high quality samples from solution methods will require complex solvent systems (including multiple aforementioned solvents as well as additional additives), which can lead to the multi-level presence of impurities, lattice distortions, and the non-uniformity of the resultant films as well as the residual solvent within the lattice which can act as a center to develop material degradation. Thirdly, for applications such as X-ray detection, thermoelectrics, and other top-down manufacturing-oriented applications, bulk samples with large volume are needed. However, solution methods make the synthesis time-inefficient because of the low crystalline growth rate and yield (low-yield (10–35%) and time-consuming (0.1–10 $\mathrm{mm^3\ h^{-1}}$)).[4]

The solution-processed methods for perovskite mainly involve two approaches, one-step deposition and two-step deposition. In one-step deposition, the perovskite formation process can be explained by the classical nucleation/growth crystallization mechanism, which includes three stages: supersaturation of the solution, nucleation, and crystal growth,

---

[a] *Ministry of Education Key Laboratory of Micro/Nano Systems for Aerospace, Northwestern Polytechnical University, 127 Youyi Road, Xi'an 710072, China. E-mail: yetao@nwpu.edu.cn*

[b] *Department of Materials Science and Engineering, Pennsylvania State University, University Park, PA, 16802, USA. E-mail: kqw5449@psu.edu*

which can be explained by the LaMer model (Fig. 1a).[5–7] A supersaturated solution is a prerequisite for nucleation. Heating and other solvent evaporation acceleration processes can facilitate the supersaturation process to saturation (C_S). As the solvent continues to evaporate, the process of crystal nucleation begins once the solution reaches supersaturation ($C^{\text{nu}}_{\text{min}}$), and the nucleation rate increases with increasing supersaturation. It is worth noting that once the crystal nucleus is formed, crystal growth begins immediately (Fig. 1b). In Fig. 1b, upon entering the third stage after entering supersaturation, the crystal nucleus begins to grow, and the growth rate increases sharply with increasing supersaturation concentration. Finally, as the solute is continuously consumed and the concentration drops below $C^{\text{nu}}_{\text{min}}$, the nucleation process stops, and the crystal continues to grow. In classical nucleation theory, the nucleation rate (N) is affected by the nucleation factor (P) and the probability of atomic diffusion (G), so eqn (1) follows:

$$N = P\Gamma = \left\{\frac{C_0 KT}{3\pi\lambda^3\eta}\right\} \exp\left(\frac{-\Delta G^*}{kT}\right) \tag{1}$$

where λ is the nucleus diameter, η is the solution viscosity and C_0 is the initial solution concentration, and ΔG^* is the critical energy barrier.

For the two-step deposition, lead halide is first deposited on the substrate, and the organic halide subsequently infiltrates the layered lead halide crystals to react and form perovskite films. However, the concentration of the organic halide affects the depth of its infiltration into the lead halide. Previous studies investigated this and found that when the concentration of MAI is below 8 mg mL^{-1}, the reaction proceeds according to eqn (2) and perovskite is generated *in situ*. When the concentration of MAI is >10 mg mL^{-1}, MAI rapidly reacts with the surface PbI_2 to form perovskite crystals, which prevents further reaction between MAI and the underlying PbI_2. When the concentration of MAI further increases to above 20 mg mL^{-1}, the surface PbI_2 still undergoes reaction (eqn (2)). However, the underlying PbI_2 reacts according to eqn (3) and (4), and the resulting supersaturated $PbI_4{}^{2-}$ recrystallizes with MA^+ to form $MAPbI_3$ perovskite (Fig. 1c).[8]

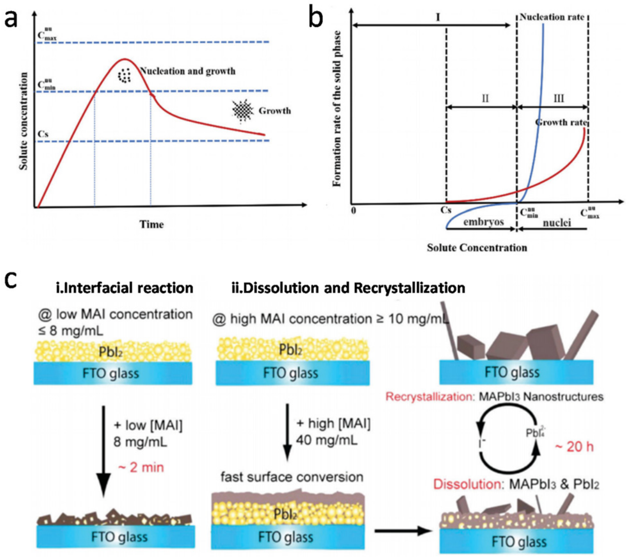

Fig. 1 (a) Schematic nucleation and subsequent growth processes. (b) Schematic relations of the nucleation and growth rates with solute concentration. Reproduced with permission.[9] Copyright 2019, Royal Society of Chemistry. (c) Schematic of the two growth mechanisms in two-step deposition methods for crystalline $MAPbI_3$ perovskites. (i) Solid–liquid interfacial reaction mechanism at a lower MAI concentration, and (ii) dissolution–recrystallization growth mechanism at a higher MAI concentration. Reproduced with permission.[8] Copyright 2015, American Chemical Society.

$$PbI_2(s) + MA^+(sol) + I^-(sol) \rightarrow MAPbI_3(s) \tag{2}$$

$$MAPbI_3(s) + I^-(sol) \rightarrow MA^+(sol) + PbI_4{}^{2-}(sol) \tag{3}$$

$$PbI_2(s) + 2I^-(sol) \rightarrow PbI_4{}^{2-}(sol) \tag{4}$$

The high boiling point of various solvents slows down the evaporation rate of the solvents,[9] making it difficult for crystallization. A multi-solvent strategy can optimize the proceeding of the supersaturation. While on the other hand, the solute–solvent interactions are different for each precursor component and solute–solvent interactions can also alter the final product(s) composition,[10–17] making the resultant film rather non-uniform. Additional solvent-related issues include (i) residual solvent in the final perovskite due to the high boiling point and strong interaction with precursor,[18] (ii) solvent-induced crystal imperfection such as the presence of a large population of point defects, lattice distortion, surface traps, and grain boundaries,[19–25] (iii) additional requirements for energy/effort input (that is, additional energy and procedures are needed to remove the solvent which further introduces more non-uniformity during these operations).[19,26]

In contrast, the "solvent-free" method can circumvent all the aforementioned issues. Compared to the mainstream solution (wet chemistry) method, the solvent-free method has been less investigated, and there are only two main methods which are classified into (i) mechanochemical synthesis and (ii) vapor-based deposition. Mechanochemical synthesis was first mentioned in 1820 by Faraday who reduced AgCl to Ag using Zn, Cu, Sn, or Fe, by grinding with a pestle in a mortar without solvent.[27] Afterwards, this method was employed for large-scale preparation of pure metal clusters, supported nanoparticles, metal–organic frameworks (MOFs), and covalent organic frameworks (COFs).[1] Recently, several examples of perovskite synthesis through the mechanochemical method have proposed a new solvent-free route for obtaining high-quality perovskites. The vapor-based deposition method has also been attempted due to its great reliability and reproducibility. The high vacuum environment ensures a low concentration of moisture and oxygen in the final products, effectively addressing the residual solvent issue typically encountered in solution-processed counterparts. The low moisture and oxygen concentration contributes to improved material stability, resulting in a longer device lifetime.[28] Furthermore, the absence of residual solvents can potentially resolve crystal quality issues caused by solvent remnants, which have a detrimental impact on device performance. This is how in commercial organic light emitting diodes (OLEDs) the organic fluorescent dye as the active layer for the device is deposited, as solution-processing cannot perfectly solve the residual solvent-induced instability issue for the organics in industry.[29]

Mechanochemical synthesis method

Fig. 2 compares the solution-processed synthesis and mechanochemical synthesis methods. Taking a classic $MAPbI_3$ (*i.e.*, $CH_3NH_3PbI_3$) as an example, in the solution-processed synthesis, the perovskite films can be formed in the spin coater within a closed chamber (Fig. 2a). After the corresponding solution is dropped onto a substrate (*e.g.*, in a two-step method PbI_2/DMF and CH_3NH_3/IPA (isopropyl alcohol) are sequentially dropped), the stage spinning can accelerate the solvent evaporation. In the meantime, annealing is needed to further remove the solvent in order to proceed the crystallization *via* the supersaturation route (Fig. 2b & c).[30,31]

However, the surface uniformity of the perovskite film will be affected by the inhomogeneous solvent evaporation, nucleation, and crystal growth over the whole substrate. The larger the substrate, the greater the inhomogeneity, thus reducing the film uniformity. In Heo *et al.*'s work, they demonstrated the lack of uniformity in the formation of perovskite film using the spin coating technique.[32] In Fig. 2d and e, SEM images of three locations from the center to the edge reveal noticeable structural irregularities in the $CsPbI_2Br$ perovskite as a function of the distance from the center of the spin-coating. This suggests that as the distance from the center increases, there is a greater variation in crystal morphology, with a higher occurrence of pinholes, ultimately resulting in reduced film uniformity. The low solubility of inorganic perovskite precursors and their rapid crystallization pose a challenge in controlling the simultaneous growth of perovskite films at different positions on a large substrate during the spin-coating process.[33–35]

Compared to the solution method, mechanochemical synthesis can exclude the solvent involvement throughout the whole synthesis. Fig. 2f & g show the sequential process of the traditional mechanochemical method. There are two sub-processes: ball milling and solidification. The conventional ball milling process needs a bowl and a set of grinding balls that are made of high-hardness materials (Fig. 2f). When the ball mill rotates according to a certain direction and angular velocity, the precursors are crushed by the collision of balls. At the same time, plastic/elastic deformations and eventually fractures occur, which produce dislocations that react together to form the product (Fig. 2g).[36,39] By adjusting the rotation speed and the size of the grinding balls, the energy input and the size of the crystallites can be fine controlled.[40] Although the all-solid-state method does not involve any solvents, the ball-milled particles usually display non-uniform sizes ranging from the nanometer-to-micrometer scales. Throughout the mechanochemical synthesis (ball-milling) process, there are still some limitations in the compatibility with film fabrication, the prepared powder is eventually dissolved in a solvent and spin-coated into a film. Another promising alternative is to melt the powder (prepared by ball milling) and then cool it to crystallize the perovskite.

In 2018, Posudievsky *et al.* reported the synthesis of $CH_3NH_3PbI_2Br$, $CH_3NH_3PbI_{3-x}Cl_x$, and $(C_6H_{13}NH_3)_2PbI_2X_2$ (X = Cl, Br, I) hybrid perovskites by a solventless ball milling treatment of the mixture of lead iodides and alkylammonium halides.[41] In particular, the $CH_3NH_3PbI_2X$ perovskite crystal particles were uniform in regard to shape and size (below 70 nm). Besides, mechanochemically prepared hybrid perovskites can be flexibly adapted to have different organic cations (*via* simply changing the precursor chemicals), and series of materials can be provided for photoelectrical fundamental studies. For example, through these methods, it has been discovered that the corresponding photoluminescence wavelength is dependent on the size of the organic cation and the type of halide ion. In 2019, Palazon *et al.* combined the ball milling method and single-source vapor deposition (SSVD) method to prepare uniform pinhole-free $Cs_3Cu_2I_5$ films.[37] This method, to some extent, solved the problem of incompatible film fabrication within the single mechanochemical synthesis method. Specifically, after the precursors were mixed in a certain stoichiometric ratio and ball-milled to obtain the powder, they prepared the perovskite films by two methods for a comparison study: solution spin coating *vs.* thermal single-source vacuum deposition. The films obtained by the spin-coating method showed significant inhomogeneity due to the limited solubility of the inorganic metal halides in organic solvents, whereas the films deposited by single source deposition exhibited a good homogeneity (Fig. 2h). However, contamination caused by the grinding balls was found during the ball milling process. The generation of contamination might be controlled by optimizing the synthesis conditions (powder-to-ball weight ratio and whether the same grinding balls and bowl had been used previously). In 2020, Morales-Masis *et al.* optimized the technique by combining mechanochemical synthesis with pulsed laser deposition (PLD) for the preparation of black γ-$CsSnI_3$ films (Fig. 2i).[38] Equimolar amounts of CsI and SnI_2 were placed in an argon-filled vessel for ball milling, and the mixed powder was obtained by grinding. The powder was then rolled into disk-shaped samples in a uniaxial press and the samples were exposed to an isostatic pressure of 360 MPa. The isostatic pressing could create a compact and dense target which was suitable for PLDs, so no further heating and sintering were required. Finally, the obtained samples were placed in a vacuum chamber for PLD single-source deposition for the perovskite films. Fig. 3a shows a bright-field TEM (transmission electron microscopy) image of the dense $CsSnI_3$ film with elongated grain particles. This study also proved that Cs, Sn, and I were uniformly distributed throughout the $CsSnI_3$ film, which could be evaluated using cross-section energy-dispersive X-ray (EDX) spectroscopy mapping (Fig. 3b).

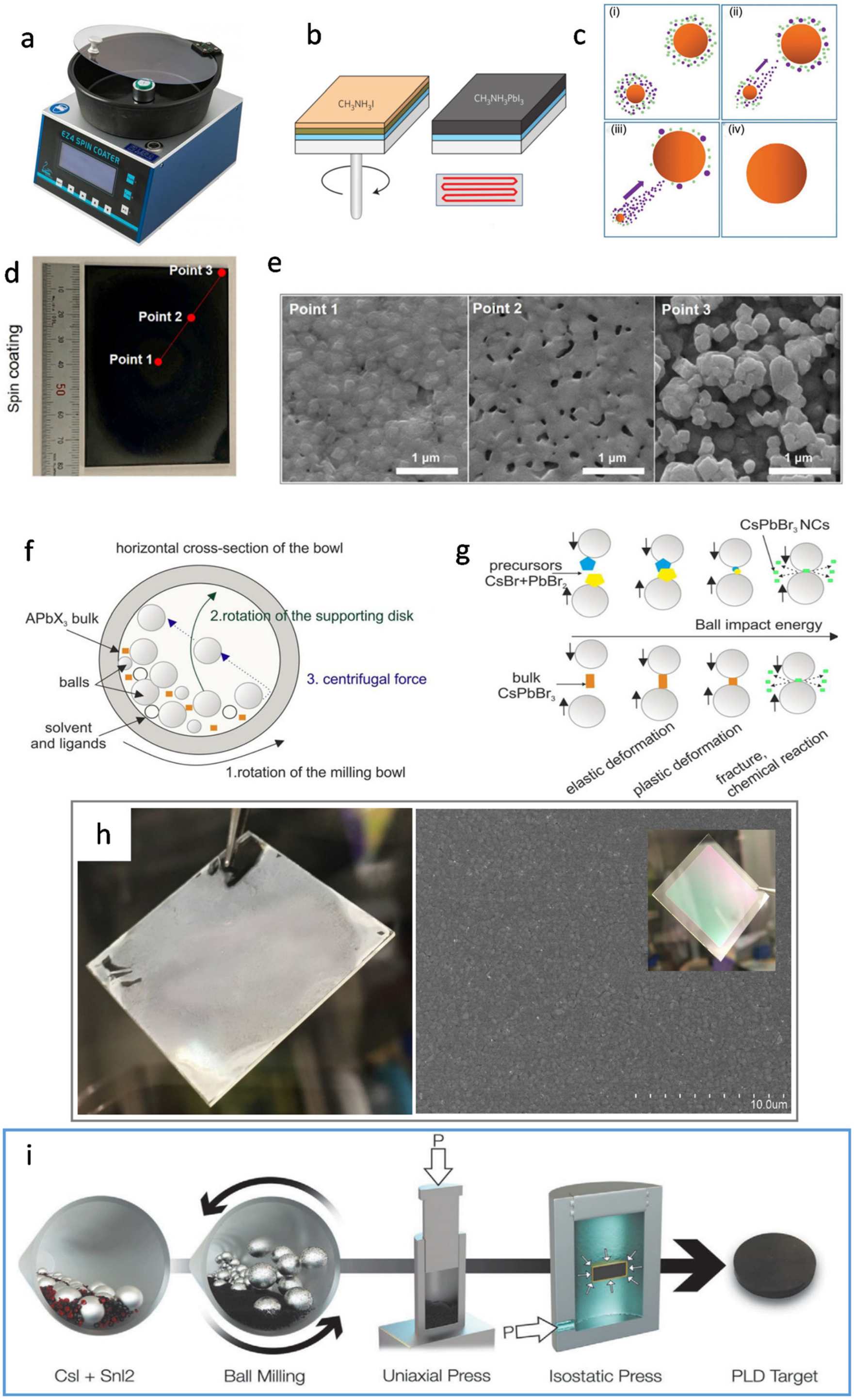

Fig. 2 (a) Photograph of the spin coater. (b) The two-step deposition method in the solution-processed method. Reproduced with permission.[31] Copyright 2014, Springer Nature. (c) Schematic of the Ostwald ripening model, showing the dynamic coarsening process of the perovskite grains with annealing time: (i) initial stage, (ii) early stage, (iii) middle stage, (iv) final stage. Reproduced with permission.[30] Copyright American Chemical Society. (d) Photograph of $CsPbI_2Br$. (e) SEM images of different locations of the thin film formed by spin coating. Reproduced with permission.[32] Copyright 2021, Elsevier Inc. (f) Cross-section of a ball mill under operation. Reproduced with permission.[36] Copyright 2018, American Chemical Society. (g) Schematic of processes that initiate a mechanochemical reaction. Reproduced with permission.[36] Copyright 2018, American Chemical Society. (h) Photograph of spin-coated inhomogeneous $Cs_3Cu_2I_5$ film (left) and SEM image and photograph (inset) of SSVD-film of $Cs_3Cu_2I_5$ showing good homogeneity (right). Reproduced with permission.[37] Copyright 2019, American Chemical Society. (i) Illustration of the PLD target fabrication process. From left to right: Stoichiometric mixture of CsI and SnI_2 powders, ball milling, uniaxial press applying 33 MPa and hydraulic press applying 360 MPa isostatically, and final target.[38] Reproduced with permission. Copyright 2020, Wiley-VCH.

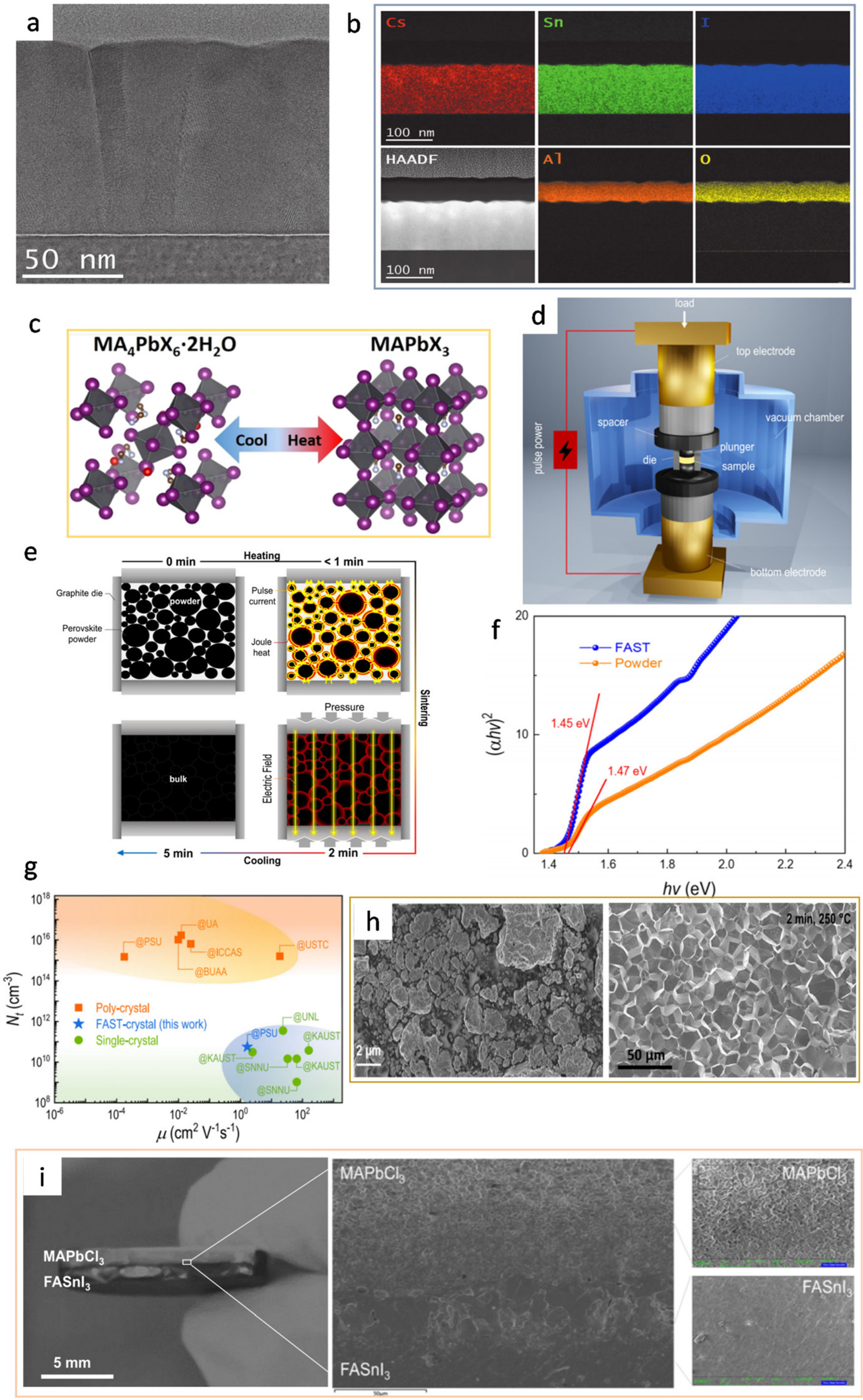

Fig. 3 (a) Cross-section bright-field TEM image of a PLD-grown black γ-$CsSnI_3$ film on Si. Reproduced with permission.[38] Copyright 2020, Wiley-VCH. (b) High-angle annular dark-field (HAADF) image and EDX mapping of the constituent elements of $CsSnI_3$ and the Al_2O_3 capping layer. EDX confirms uniform distribution of Cs, Sn, and I along the thickness of the layer and conformal coating of the Al_2O_3 capping layer. Reproduced with permission.[38] Copyright 2020, Wiley-VCH. (c) Schematic of the reversible transformation between $MA_4PbX_6 \cdot 2H_2O$ and $MAPbX_3$. Reproduced with permission.[42] Copyright 2021, American Chemical Society. (d) Schematic of the FAST equipment. Reproduced with permission.[4] Copyright 2022, Springer Nature. (e) Processing diagram showing the solid densification of halide perovskites in a graphite die. Reproduced with permission.[4] Copyright 2022, Springer Nature. (f) Tauc plot for powder and FAST-$MAPbI_3$. Reproduced with permission.[4] Copyright 2022, Springer Nature. (g) Comparison of trap density and mobility between FAST-$MAPbI_3$ and state-of-the-art solution-processed thin film and single crystal of $MAPbI_3$. The orange square, blue star, and green circle represent the poly-crystal, the FAST-crystal, and the single crystal, respectively. Reproduced with permission.[4] Copyright 2022, Springer Nature. (h) SEM images of the ball-milled $MAPbI_3$ (left) and FAST-$MAPbI_3$ (right). Reproduced with permission.[4] Copyright 2022, Springer Nature. (i) Photo of the bilayer heterojunction of $MAPbCl_3$ and $FASnI_3$, magnified cross-sectional SEM at the heterointerface, showing an intimate interface between the two perovskites. Reproduced with permission.[4] Copyright 2022, Springer Nature.

Solvent-free mechanochemical synthesis can also be used to prepare degradation or by-products of 3D perovskite counterparts, which can be converted to perovskite by certain treatments. In 2021, Palazon *et al.* synthesized 0D $MA_4Pb(Br_{1-x}I_x)_6 \cdot 2H_2O$ powders by ball milling, and demonstrated $MA_4PbI_6 \cdot 2H_2O$ reversible transformation to a 3D perovskite analog ($MAPbI_3$) by controlled (de)hydration under thermal annealing and simple cooling in humid air conditions (Fig. 3c).[42] Based on the conventional mechanochemical (ball milling) method, our group recently reported a new electrical and mechanical field-assisted sintering technique (EM-FAST, FAST for simplicity) for the preparation of high-quality perovskite.[4] The whole process was operated in an airtight chamber consisting of a mechanical loading system with a high-power electrical circuit in a controlled atmosphere (Fig. 3d). Perovskite powder (by ball milling) was fixed in the die which was quickly heated to a high temperature by a high pulse current (1–10 kA). Meanwhile, the opposite static mechanical stress was applied simultaneously up and down to compress the sample. Through rapid heating and compressing, the powder sample could transform into a solid bulk crystal (Fig. 3e). Certain properties of FAST-$MAPbI_3$ are similar to single crystals. According to the Tauc plot (Fig. 3f), the optical bandgap of FAST-$MAPbI_3$ was calculated to be 1.45 eV, which is closer to the optical bandgap of a single crystal (1.51 eV) than to the typical thin film optical bandgap (1.6 eV). Using single carrier space charge limited current (SCLC) theory, the calculated trap density and hole mobility of FAST-$MAPbI_3$ are 5.4×10^{10} cm^{-3} and 1.7 cm^2 V^{-1} s^{-1}, respectively. These values of FAST-$MAPbI_3$ are located in a region closer to the single crystals rather than typical polycrystalline films in the trap density–mobility plot (Fig. 3g), and the trap density is significantly lower than that of solution-processed $MAPbI_3$. Trap density and hole mobility can be expressed by the equations:

$$V_{\mathrm{FTL}} = \frac{e n_{\mathrm{trap}} L^2}{2\varepsilon_0 \varepsilon} \tag{5}$$

$$J = \frac{9}{8}\varepsilon_0 \varepsilon_{\mathrm{r}} \mu \frac{V^2}{L^3} \tag{6}$$

$$\mu = \frac{8JL^3}{9\varepsilon_0 \varepsilon_{\mathrm{r}} V^3} \tag{7}$$

where V_{TFL} is a voltage threshold for current flow, e the elementary charge, ε_0 and ε_{r} are the relative permittivity of free space and perovskite, n_{trap} is the trap density, and L is the sample thickness. V_{TFL} is a measurable quantity and a known value, and the trap density n_{trap} can be obtained from eqn (5). In eqn (6) and (7), V is the voltage and J is the current density. Compared with the crystal density obtained from the ball milling method, the perovskite synthesized by the FAST technique had a more compact crystal film with a controllable grain size (Fig. 3h). The FAST synthesis of perovskite upgrades the conventional mechanochemical method in film formation with a sintering technique and makes a heterojunction-structured perovskite possible, while reports about the ultrathick hetero-bilayer of halide perovskites are rare at this early research stage. Fig. 3i shows an intimate interface between different perovskites in the magnified cross-sectional scanning electron microscope (SEM) images at the heterointerface. The FAST technique might be a promising way to alloy halide perovskites with solid materials (*e.g.*, metal and carbon) which cannot be processed *via* the traditional solution method.

Vapor vacuum deposition methods

In addition to mechanochemical synthesis methods, vapor-based synthesis methods also play an important role in the solvent-free synthesis of the perovskite films, and have been continuously developed and improved in the past decade. The vapor-deposition method was first applied to prepare layered perovskite crystals in 1997. Tsutsui *et al.* demonstrated the early possibility of preparing layered and cubic perovskites by dual-source vapor deposition of lead iodide and organic ammonium iodide.[43] Later, many researchers noticed that the excellent properties of perovskites allowed them to use alternative materials for solar cells. The power conversion efficiency (PCE) of the perovskite solar cells (PSCs) has improved from 15.4% in the first work about vapor-deposited PSCs to 24.24% in the latest research results in 2022.[44,45] Although the PCE of the vapor-processed PSCs is slightly inferior to that of the solution method-based devices, the precise regulation of the film's composition, crystallinity, thickness, uniformity, and other parameters indicate that the vapor-processed method shows great potential in massive and large-area fabrication of perovskite thin films in the future.

In general, the core of the vapor-based method is to obtain the gas phase state of the required components by heating evaporation or sublimation, and then precisely controlling the process of vapor deposition onto the substrate in a high or low vacuum chamber. In view of the different deposition sequences of various precursor components in the vapor-based methods, researchers have developed two deposition techniques: co-evaporation deposition and sequential evaporation deposition. Here, we list the representative cutting-edge progresses in these scenarios with regard to high-quality samples.

The co-evaporation method has demonstrated good controllability of the performance of the perovskite, whereby the optimization of perovskite performance can be achieved by artificially changing the content of certain components within the film. It has been proved that both the different halide elements (Cl^-, Br^- and I^-) and the different cations (Cs^+, MA^+, and FA^+) showed impacts on the comprehensive properties of the perovskite films. Although the co-evaporation method has shown outstanding advantages in the preparation of perovskite films, the controllability and real-time monitoring in the process of co-evaporation are still a challenge, especially for the control of the evaporation rate of multiple precursors and the monitoring of film thickness. In a typical co-evaporation method, several quartz-crystal-monitors (QCMs) are fixed near the crucibles with precursors or substrate to simultaneously monitor the deposition status of multiple precursors and the thickness of the layers. Different precursors may interfere with each other's QCM readings during evaporation, especially when precursors with similar properties are being evaporated simultaneously. Thus, the monitored evaporation rates are not highly reliable, and film thickness and deposition rates are often over- or under-estimated, ultimately affecting film quality, resulting in reduced device performance.[46,47] To solve this problem, layer-by-layer sequential vapor deposition is an alternative technique that can obtain high-quality and homogeneous perovskite films for the fabrication of high-performance devices, while avoiding the risk of cross-contamination of lead halide and organic ammonium salts.[45]

Organic cation perovskite

In 2013, Snaith *et al.* reported the deposition of $CH_3NH_3PbI_{3-x}Cl_x$ film with a dual-source co-evaporation technique.[44] The perovskite absorbers were deposited simultaneously through dual-source evaporation from lead chloride ($PbCl_2$) and methylammonium iodide (CH_3NH_3I) onto the TiO_2-compact-layer-coated fluorine-doped-tin-oxide (FTO) substrates (Fig. 4a). Two sensors directly above the evaporation source monitored the evaporation rates of the two materials, as the film quality was very sensitive to the relative ratio of CH_3NH_3I to $PbCl_2$ and the overall deposited thickness. The deposited films were extremely uniform and appeared to be crystalline in length scales of hundreds of nanometers, whereas the solution-processed films exhibited numerous deep voids and only partially coated the substrate (Fig. 4c). Similarly, the cross-sectional image of the vapor-deposited perovskite (Fig. 4d) showed good flatness with an average thickness of ~330 nm, while the solution-processed perovskite film showed an undulating nature with thickness varying from 50 to 410 nm. This remarkable difference in film quality would be more remarkable in large-scale fabrication. In 2014, Lin *et al.* prepared $MAPbI_3$ perovskite using a layer-by-layer vacuum sublimation technique under 100 °C.[46] It was demonstrated that PbI_2 was *in situ* converted to perovskite during the sequential deposition process. Li *et al.* reported a layer-by-layer vacuum deposition technique for perovskite.[48] By alternating the $PbCl_2$ and MAI precursor layers, they obtained $MAPbI_{3-x}Cl_x$ devices with an average PCE of 16.03%. Compared with co-evaporation methods, the layer-by-layer vapor deposition technique simplifies the deposition rates and thin film composition. Bolink *et al.* prepared $MAPb(Br_xI_{1-x})_3$ perovskites with three-source co-sublimation of MAI, lead iodide (PbI_2), and lead bromide ($PbBr_2$) in 2018 (Fig. 4b).[49] The evaporation rates of PbI_2 and $PbBr_2$ were controlled by adjusting the temperatures of the crucibles. The deposition rate of $PbBr_2$ with respect to PbI_2 was increased while the rate of MAI remained constant, and the prepared champion devices based on $MAPb(Br_{0.2}I_{0.8})_3$ and $MAPb(Br_{0.5}I_{0.5})_3$ showed different photovoltaic properties (open-circuit voltages (V_{oc}) of 1.080 V, 1.128 V; fill factors (FF) of 80.7%, 79.3%; PCEs of 14.7%, 5.5%, respectively).

In 2019, Fan *et al.* proposed a special sequential vapor deposition method to deposit uniform mixed-cation mixed-halide ($MA_yFA_{1-y}PbI_xBr_{3-x}$) perovskite films. The devices fabricated based on this strategy showed a PCE of 15.14% (Fig. 4e).[50] Moreover, the implementation of sputtered SnO_2 films as the electron transport layer (ETL) was firstly demonstrated. Before the evaporation, PbI_2 and $PbBr_2$ with an optimized ratio were mixed in one crucible, and as their boiling points were quite close, they could both be fully evaporated. Subsequently, the MA and FA could also be fully evaporated at a very similar rate. In each step, only one crucible was heated to vaporize the precursor, so only one QCM was used to detect the evaporation rate, avoiding the usage of multiple sources.

The ratio between precursors is an important parameter to tune the final crystal quality. For example, Johnston *et al.* quantified the influence of excess PbI_2 on the vapor deposition process of high-quality $MAPbI_3$ formation.[51] Excess PbI_2 could not only make the bulk or grain boundaries directly passivated, but it also promotes the growth of perovskite crystals with better carrier properties. In addition, excess PbI_2 greatly enhanced the absorption of MAI. When only MAI was deposited, there was no MAI on the FTO or glass substrates. The quartz microbalance thickness monitors also proved that the absorption of MAI near the PbI_2 substrate was obviously higher than that in PbI_2-free areas. Notably, the residual PbI_2 made contributions to the photocurrent improvement while the unreacted PbI_2 might lead to the photoinstability of the perovskite films.[52,53] These carrier transport features can be further tuned through surface treatment.

Bruno *et al.* implemented a new surface treatment strategy to improve charge carrier transport at the grain boundaries within the $MAPbI_3$ film.[54] It has been demonstrated that a few intrinsic point defects such as Pb–I anti-site defects (PbI_3^-) could be found after the evaporation of organic cations and halides.[55] To minimize the adverse effects on film quality, they introduced K^+ from potassium acetate (KAc) to improve grain boundary conductivity through the immobilization of uncoordinated species. K^+ could permeate deeply and homogeneously in thick $MAPbI_3$ films, and the conductivity of the films was improved with deeper penetration (Fig. 4f). The combination of MAI and KAc could also improve the film morphology, which was reflected by reduced pinholes and increased particle size of the perovskite crystals (Fig. 4g). In 2021, Liu *et al.* prepared large-area perovskite films on rigid (400 cm^2, Fig. 4i) and flexible (300 cm^2, Fig. 4j) substrates by sequential vapor deposition (Fig. 4h).[56]

Due to the easiness in the preparation of large-area perovskite films with the vapor method, $MAPbI_3$ was the preferred perovskite material for research in the beginning. However, the intrinsic instability of MA^+ to thermal stress and the ambient air conditions limit the reliability of $MAPbI_3$-based devices under high-temperature conditions and in other complex environments.[57–59] Formamidinium iodide (FAI)-based perovskite absorber layers with superior thermal stability have become the preferred choice for the fabrication of single-junction PSCs, and PCEs over 25% were achieved for FA-

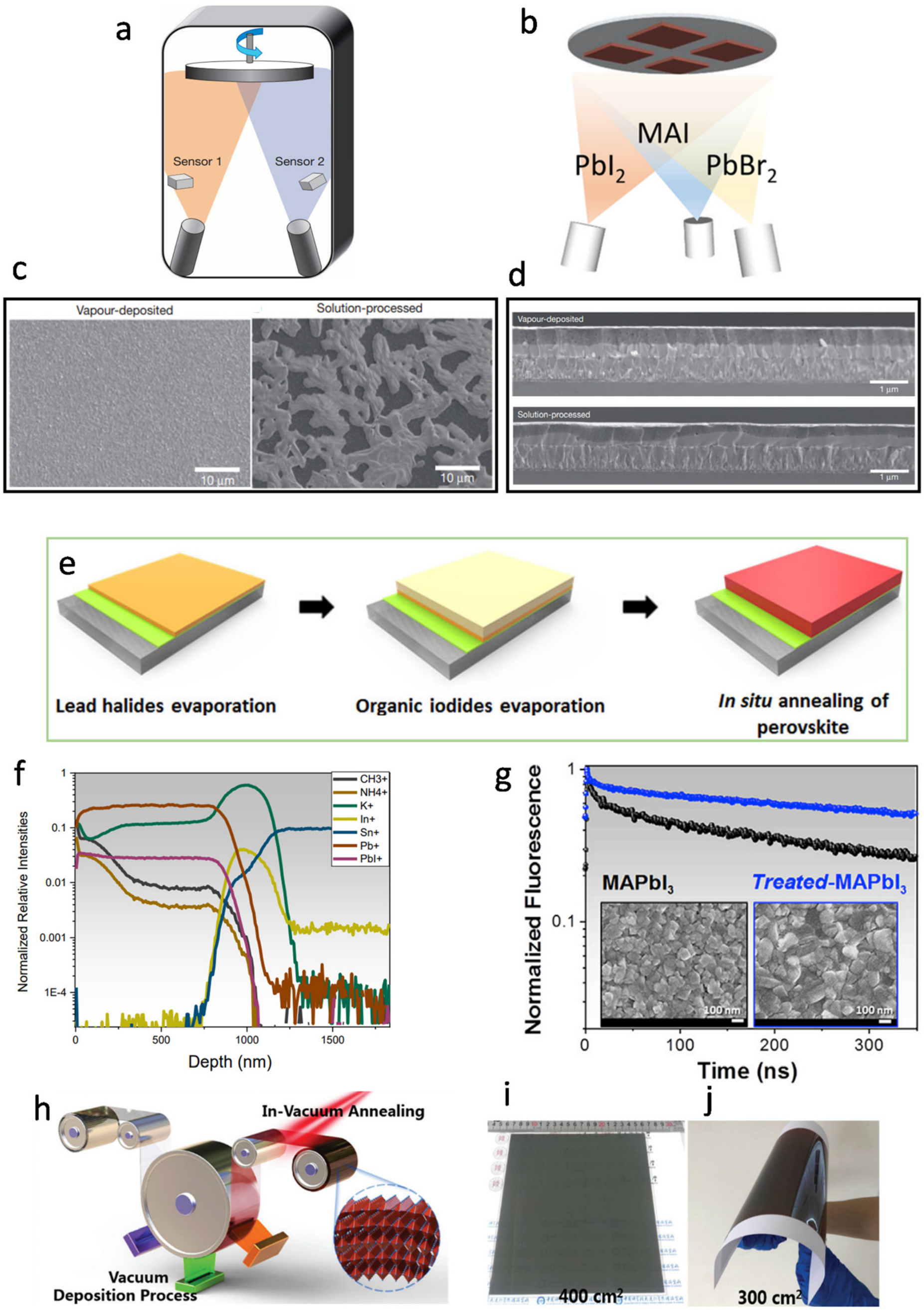

Fig. 4 (a) Schematic of the dual-source thermal evaporation system for depositing the perovskite absorbers, the left source was methylammonium iodide, and the right source was $PbCl_2$. Reproduced with permission.[44] Copyright 2013, Springer Nature. (b) Schematic of three-source co-evaporation of the perovskite films. Reproduced with permission.[49] Copyright 2017, American Chemical Society. (c) SEM top views of a vapor-deposited perovskite film and a solution-processed perovskite film. Reproduced with permission.[44] Copyright 2013, Springer Nature. (d) Cross-sectional SEM images under lower magnification of completed solar cells constructed from a vapor-deposited perovskite film and a solution-processed perovskite film. Reproduced with permission.[44] Copyright 2013, Springer Nature. (e) Schematic illustration of the fabrication procedures of an all-vacuum-deposited perovskite film. Reproduced with permission.[50] Copyright 2019, Wiley-VCH. (f) The depth profile for the positive ions (CH_3^+, NH_4^+, K^+, In^+, Sn^+, Pb^+, PbI^+) on a treated-$MAPbI_3$ film deposited on $PCBM/SnO_2/FTO$ glass substrate. Reproduced with permission.[54] Copyright 2020, Elsevier Inc. (g) TRPL decays and top-view SEM images of pristine $MAPbI_3$ (black line) and treated-$MAPbI_3$ (blue line). Reproduced with permission.[54] Copyright 2020, Elsevier Inc. (h) Schematic of multisource vacuum deposition with an in-vacuum annealing process for large-area perovskite films; photographs of FA-based perovskite films deposited on (i) glass and (j) flexible polyethylene terephthalate (PET) substrates. Reproduced with permission.[56] Copyright 2021, Royal Society of Chemistry.

based PSCs by the solution-based deposition method.[60–65] Researchers paid more attention to perovskites containing Cs^+ and FA^+ for their superior long-term stability and high PCEs.[66–71] Additionally, the incorporation of CsI in perovskites resulted in high quality perovskite films without pinholes and improved the stability of flexible PSCs (after 400 bends at a radius of 4 mm, the PCE remained ~94% of the initial value).[72]

Organic–inorganic cation perovskite

In 2017, Liu *et al.* reported the fabrication of pin-hole-free cesium substituted perovskite films by a vacuum co-evaporation method, and the $MA_{0.77}Cs_{0.23}PbI_3$ PSC exhibited a PCE of 20.13%, increased by ~27% as compared to the pristine $MAPbI_3$ based devices.[73] To study the effect of Cs substitution on the crystallization of the $MAPbI_3$ film, X-ray diffraction (XRD) was utilized to characterize the perovskite films with different Cs amounts (0, 0.11, 0.17, 0.23 and 0.34). In the magnified version of the (110) diffraction peak of $MA_{1-x}Cs_xPbI_3$, the 2θ monotonously moves from 14.14° to 14.36° with Cs content increasing from 0 to 0.34 (Fig. 5a), which proved that Cs cations could be integrated into the $MAPbI_3$ lattice. Moreover, with the increase in Cs cation content, the bandgap of $MA_{1-x}Cs_xPbI_3$ was enlarged linearly (Fig. 5b) and the absorption peak shifted to shorter wavelength (Fig. 5c), demonstrating that the band gap of $MA_{1-x}Cs_xPbI_3$ can be fine-tuned by the Cs substitution. The prepared Cs-substituted PSCs show higher stability than typical $MAPbI_3$-based devices with the PCE decreased by only 4.37% of the initial efficiency after the PSCs were stored in the dark for one year. The high stability of the Cs-substituted PSCs could be attributed to the high purity of the crystalline phase, low trap-state density, reduced lattice constant and relaxed strain after the incorporation of Cs.[48,74]

In 2018, Bolink *et al.* first reported the preparation of multi-cations/anions perovskite compounds using a multiple sources (3 or 4) thermal vacuum deposition method (Fig. 5d).[75] However, the uniformity of the films was poorer than that of the samples obtained by simple vacuum vapor deposition methods, indicating that more research was needed to control the morphological homogeneity in the multi-source co-deposition method. Similar results about the effect of excess PbI_2 were observed in FA based perovskites by Stranks *et al.* in 2020.[76] In the fabrication of $FA_{0.7}Cs_{0.3}Pb(I_{0.9}Br_{0.1})_3$ films, excess PbI_2 enhanced the film stability and photoelectric properties, yielding longer carrier lifetimes and high photoluminescence quantum efficiency (PLQE). The resultant PSC showed a stable PCE of 18.2% which was the highest performance for the vapor-deposited MA-free system. Li *et al.* obtained a high-quality $Cs_{0.24}FA_{0.76}PbI_{3-x}Br_x$ film with 4 nm SrI_2 to accelerate the conversion rate of PbI_2 to perovskite, and the film showed large grain sizes, and low trap-state density.[77] This indicates that a moderate amount of SrI_2 could promote the conversion of PbI_2 to perovskite and achieve a champion PCE of 17.66% with a high FF up to 0.79. Later in 2021, Bolink *et al.* showed the preparation of $FA_{1-n}Cs_nPb(I_{1-x}Br_x)_3$ samples by four-source evaporation under room temperature.[78] The bandgaps of the perovskites were tuned between 1.7 eV and 1.8 eV by controlling the amount of bromide and cesium, and the champion PSC exhibited a PCE of 16.8% and retained 90% of its initial efficiency after 2 weeks of continuous operation.

Inorganic cation perovskite

In 2017, Chen *et al.* reported that they had successfully grown controllable and large-area continuous single-crystalline $CsPbBr_3$ thin films on $SrTiO_3(100)$ substrates by a facile vapor-phase epitaxy growth, as well as directionally aligned $CsPbBr_3$ nanosheet arrays (Fig. 5h).[81] The resulting single-crystalline $CsPbBr_3$ exhibits excellent crystal quality and optoelectronic properties, such as slow carrier recombination rates, low surface recombination velocities, and low bulk defect densities. Later in 2019, large-area and high-quality $CsPbBr_3$ single crystals were grown on GaN/sapphire substrates by the CVD method.[79] The $CsPbBr_3$-GaN formed a type II semiconductor heterojunction, indicating a great opportunity for developing application-level wide-bandgap perovskite micro/nano optoelectronic and photonic devices (Fig. 5e). In 2021, Zhou *et al.* found that the key to large-grain $CsPbBr_3$ crystals was to control the crystal growth rate.[80] They demonstrated the preparation of $CsPbBr_3$ crystals with a grain size of up to 3.1 mm by controlling the growth rate, which was affected by the gas flow rate and deposition location (Fig. 5f & g). In 2022, Yi *et al.* developed a Cl-alloy-mediated sequential vacuum deposition method for fabricating high-efficiency PSCs with a maximum PCE of 24.42%.[45] They demonstrated that the introduction of a moderate amount of Cl in $Cs_{0.05}PbI_{2.05-x}Cl_x$ could accelerate the solid-state diffusion of organic ammonium salt into the lead iodide lattice. Besides, Cl facilitated the crystallization of perovskite and improved the film homogeneity by the reduction of the grain boundaries.[82] It can be seen in Fig. 5i that the $PbCl_2$-alloy-mediated film shows a larger grain size under the same annealing time as compared to the plain samples, which indicated fewer defects within the prepared film, resulting in the reduction of the Shockley–Read–Hall (SRH) recombination. More importantly, the phase conversion from α- to δ-phase is one of the main drawbacks of $FAPbI_3$ perovskites and the doping of Cl promotes the transition from the δ-phase to the α-phase and reduces the amount of δ-phase within the perovskite film.[83–85]

It is important to monitor and control the evaporation rate of the precursor in the vapor phase method, while the relevant parameters of the deposited substrate, such as crystallinity, orientation, lattice parameter and morphological properties, also have a significant impact on the performance of the film.[86–88] In 2014, Lin *et al.* observed different crystalline morphologies in perovskite films deposited on substrates with different temperatures.[46] When the substrate was heated to 65 °C, only the upper part of PbI_2 reacted with MAI to form the perovskite layer, while the bottom part of the PbI_2 still remained unchanged. As the temperature gradually increased to 75 °C and 85 °C, the crystal structures were first observed to be fused together and have fuzzy domain boundaries, and the domains reappeared vividly at 85 °C but with a much smaller domain size of about 200 nm (Fig. 5j). Moreover, when the film was sublimated at 85 °C, the crystallization was not as pure as the film at a substrate temperature of 75 °C, probably due to the violent reaction of MAI and $PbCl_2$ at 85 °C. Qi *et al.*

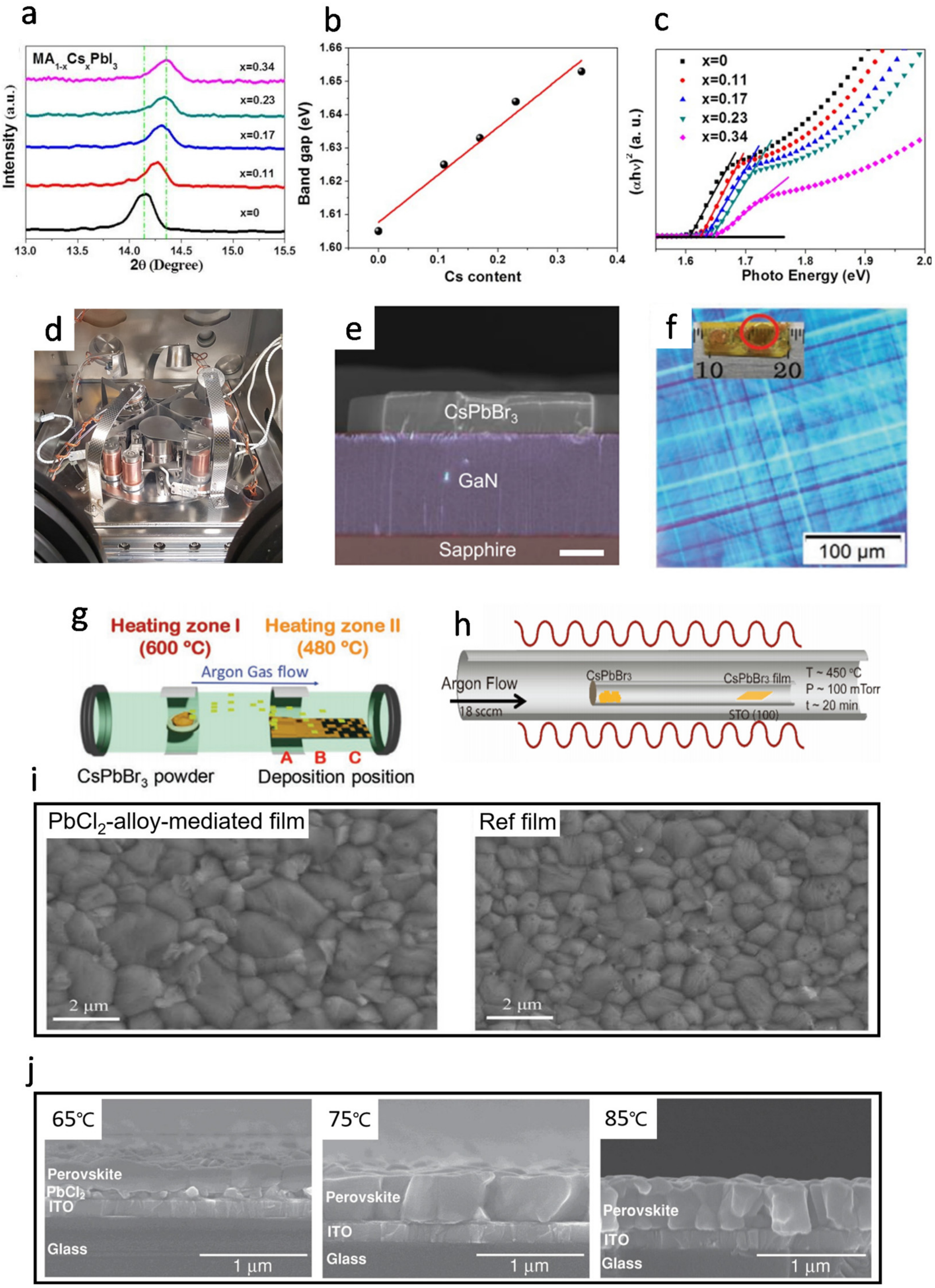

Fig. 5 (a) XRD zoomed in on (110) diffraction peaks of perovskite based on various Cs contents. Reproduced with permission.[73] Copyright 2017, Royal Society of Chemistry. (b) The linear relationship of the band gap of perovskite with Cs content. Reproduced with permission.[73] Copyright 2017, Royal Society of Chemistry. (c) The band gap of $MAPbI_3$ with different Cs content. Reproduced with permission.[73] Copyright 2017, Royal Society of Chemistry. (d) Photograph of the employed evaporation chamber. Reproduced with permission.[75] Copyright 2018, Wiley-VCH. (e) Cross-section SEM image of the $CsPbBr_3$–GaN heterojunction. The cross-section of the $CsPbBr_3$ microplatelet single-crystals (MPC) is uniform rectangular. Scale bar: 2 μm. Reproduced with permission.[79] Copyright 2019, American Chemical Society. (f) Polarized optical microscopy (OM) image for a single grain. The inset is the photograph of CVD grown $CsPbBr_3$ film with mm-scale grains. (g) Schematic illustration of CVD setup: a two-zone furnace, where the precursor is placed at zone-I, and substrate positions (marked as A, B, and C) are placed in zone-II. Reproduced with permission.[80] Copyright 2021, Wiley-VCH. (h) The tube-in-tube setup for the vapor phase epitaxial growth of the $CsPbBr_3$ nanoplates and single crystal thin films on STO substrates under higher temperature (450 °C). Reproduced with permission.[81] Copyright 2017, American Chemical Society. (i) Top-view SEM images of $PbCl_2$-alloy-mediated film and reference film. Reproduced with permission.[45] Copyright 2022, Science. (j) Top view SEM images of the perovskite thin films fabricated at substrate temperatures of 65 °C, 75 °C, and 85 °C. Reproduced with permission.[46] Copyright 2014, Wiley-VCH.

investigated the effect of substrate temperature variation on the adhesion of MAI on the substrate, and the adhesion coefficient of MAI gradually decreased with the increasing of substrate temperature, resulting in the best device performance with V_{oc} of 1.010 V, J_{sc} of 12.85 mA^{-2}, FF of 66.60%, and overall PCE of 8.64%.[89] Meanwhile, the type and chemical properties of the substrate not only affect the growth of the perovskite but also directly impact the energetics of the interface, which determines the rate of extraction and recombination of photogenerated charges in solar cells.[90] For instance, the UV photoelectron spectroscopy (UPS) spectra of $MAPbI_3$ were obtained after the increasing of the thickness of $MAPbI_3$ layer-by-layer on different substrates, such as polyethyleneimine (PEIE) and poly(3,4-ethylenedioxythiophene)polystyrene sulfonate (PEDOT:PSS). The results showed that the material characteristics of $MAPbI_3$ could be detected on (PEDOT:PSS) substrates after only 3 nm thickness. In contrast, the formation of perovskite on metal oxide substrates like MoO_3 or indium tin oxide (ITO) was only observed when the deposition thickness was 10 nm or 30 nm, respectively.[91,92]

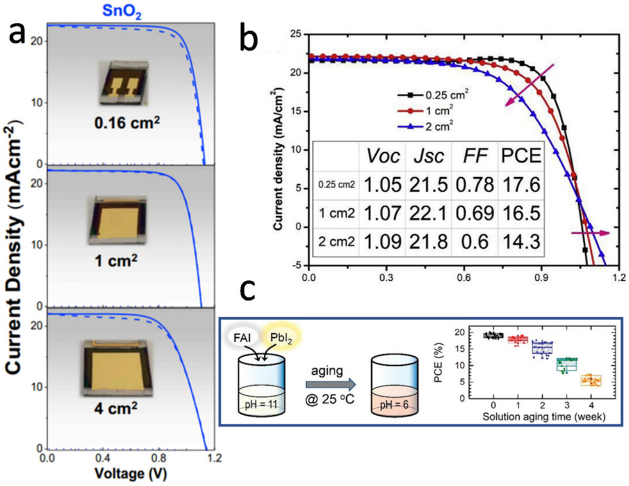

	Voc	Jsc	FF	PCE
0.25 cm2	1.05	21.5	0.78	17.6
1 cm2	1.07	22.1	0.69	16.5
2 cm2	1.09	21.8	0.6	14.3

Fig. 6 (a) Dark, forward, and backward *J*–*V* curves of treated-$MAPbI_3$ PSCs with active areas ranging from 0.16 to 4 cm^2. Reproduced with permission.[54] Copyright 2020, Elsevier Inc. (b) The *J*–*V* curves of a device with >2 cm^2 Au electrode measured with different square mask areas. Reproduced with permission.[93] Copyright 2019, Elsevier Inc. (c) Evolution of the power conversion efficiencies of $FAPbI_3$ PSCs based on the precursor solution aged for different times. Reproduced with permission.[99] Copyright 2022, Wiley-VCH.

Outlook and challenges

Benefits of solvent-free methods

Good scalability and reproducibility. The PSCs with high PCE obtained through solution methods are mostly achieved with a small area and are still limited to laboratory-scale size (<1 cm^2). As the PSCs' area increases, the decline in PCE of PSCs obtained through the solution deposition method is much faster than that of PSCs obtained by the vacuum deposition method, which shows that PSCs obtained through the vacuum deposition method exhibit excellent PCE stability. As shown in Fig. 6a, Li *et al.* reported an increase in the active area of PSCs prepared by vacuum vapor-based deposition from 0.16 cm^2 to 4 cm^2, with a decrease in the PCE decay rate of 16.67% (0.16 cm^2: 19.91%; 4 cm^2: 16.59%).[54] In contrast, in previous results reported by our team, the PCE decay rate for PSCs prepared by solution processing where the active area increased from 0.25 cm^2 to 2 cm^2 was 18.75% (0.25 cm^2: 17.6%; 2 cm^2: 14.3%) (Fig. 6b), and when the area was further increased to 4 cm^2, the decay rate would be much higher than 18.75%.[93]

The defect tolerance of metal halide perovskites refers to the predominance of shallow-level defects, which do not act as strong non-radiative recombination centers.[94] This is considered a unique characteristic of metal halide perovskites and a key reason for their high photovoltaic conversion efficiency, especially in small-area devices. However, non-radiative recombination centers and deep-level defects produced by factors such as point defects, grain boundaries, surfaces, and interfaces still reduce the PCE of PSCs, remarkably for the large area devices. As mentioned above, with increasing device area, solution processing exhibits inhomogeneity in film formation from the center to the edge, resulting in a higher number of defects and significantly lower film quality compared to vacuum deposition.[32]

In the solution processed method, the vapor pressure of the solvent is determined by temperature and humidity, and the nucleation and growth of perovskite grains are strongly affected by solvent evaporation.[95] To obtain reproducible perovskite films, it is necessary to control the temperature and humidity to be consistent throughout the experimental process. In addition, it has been proved that progressive chemical reactions occur in precursor solutions stored under an inert gas atmosphere, indicating different reaction components may participate in the preparation of perovskite films while using the same precursor solution at different times.[96–98] This may lead to significant deviations in PSC performance (Fig. 6c), which results in non-reproducibility of perovskite film quality and device performance between batches and among different laboratories.[99]

In contrast, the vacuum deposition method is solvent-free and performed under high vacuum (≈10^{-6} Torr), where atmospheric gas molecules are rare. This avoids the impact of some organic solvents in the solution method on the absorption of moisture in the environment, which may affect the quality of perovskite films. In large-scale production, after optimizing the parameters of the equipment, fixed process parameters can be used for deposition to obtain perovskite films with good reproducibility. Organic light-emitting diode (OLED) devices based on thermal evaporation technology have been successfully launched on the market. Recently, a 97-inch OLED display has been released, which supports the compatibility of thermal evaporation technology with large-area film and device fabrication.[99]

In summary, the vapor-phase methods demonstrate the potential for future preparation of large-area, high-quality, and reproducible perovskite films in multiple batches.

Precise control of stoichiometry. For the two solvent-free synthetic methods discussed in this article, namely, the mechanochemical synthesis and the vapor deposition, the chemical stoichiometry of the resulting perovskite can be precisely controlled through the following approaches. In the case of mechanochemical synthesis, the first step is to accurately control the molar ratio of the reactants by adding different precursors according to the theoretical stoichiometry. Pure phase and gram scale $CsPbBr_3$, $CsPb_2Br_5$, and Cs_4PbBr_6 can be synthesized by changing the ratio of CsBr and $PbBr_2$ (Scheme 1).[1]

High-energy ball milling can introduce energy between the powder of different reactants, thereby promoting the reaction. The degree of reaction completion and chemical stoichiometry can be controlled by adjusting the ball milling rotation speed and time. Pal *et al.* demonstrated post-synthetic solid-state transformations of $CsPbBr_3$ to $CsPb_2Br_5$, and Cs_4PbBr_6 (Scheme 2),[1] which indicated that reaction time and degree of reaction have a significant effect on the composition and structure of the reaction products. Moreover, other factors also need to be taken into consideration, such as the high temperature required for solvent-free synthesis methods, as well as knowledge of the melting points and decomposition temperatures of the precursors and different perovskite materials.[40]

Regarding the vapor deposition method, the evaporation and deposition rates of the different precursors in the vacuum chamber largely reflect the stoichiometric ratios of different elements in perovskite. In the evaporation process for organic perovskite, the vapor pressure and diffusivity of low-molecular-weight organic halides can cause unnecessary deposition on the chamber wall, which may cause additional deposition or introduction of impurities in the next vapor deposition cycle; thus, an unwanted stoichiometric ratio of perovskite can be present.[99] Recently, perovskite precursors with large molecular weight (FAI) and high sublimation temperature (CsX, X = I, Br, Cl) have been discussed to avoid this problem. Additionally, the state-of-the-art evaporators with a cooling system for the inner chamber wall can prevent redeposition of organic halides.

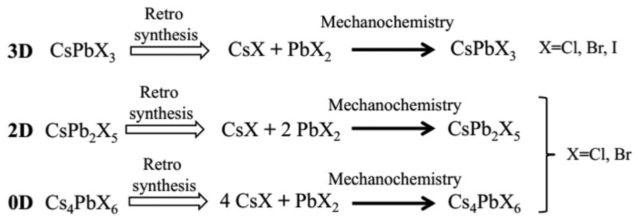

Scheme 1 Retrosynthetic approach for the synthesis of inorganic perovskite type halides using CsX and PbX_2 as solid precursors.

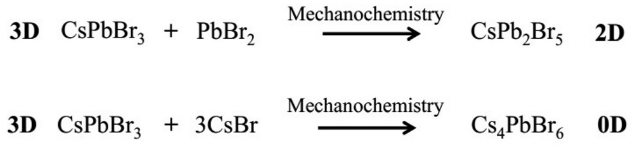

Scheme 2 Post-synthetic solid-state transformations of $CsPbBr_3$ to $CsPb_2Br_5$ and Cs_4PbBr_6.

Quartz crystal microbalances (QCM) are widely used for detecting evaporation rates of corresponding precursors. It was reported that adjusting the position of the QCM and using shielding around the QCM can prevent cross-read on sensors, thereby improving the accuracy of the measured evaporation rates of the precursors.[100] Bolink *et al.* conducted a comprehensive study of the vacuum deposition of $MAPBI_3$ perovskite and established a growth kinetic model, which could control the stoichiometry of $MAPbI_3$ during the vacuum co-deposition process. To accurately control the stoichiometry of perovskite deposited by the gas-phase method, it is necessary to establish growth kinetic models that are applicable to different materials. Roß *et al.* revealed that the stoichiometry of the deposited film was influenced by the substrate temperature which significantly affected the adhesion of MAI. High substrate temperature prevented the adhesion of MAI and may accelerate the thermal decomposition of MAI (Fig. 7).[101] Thus, a suitable substrate temperature should be set for the vacuum deposition of MAI based perovskites.

Existing challenges

Decomposition of organic component. On the other hand, there is still room for improvement in the vapor deposition method, as one of the challenges is the thermal decomposition of organic compounds within the vacuum chamber. This decomposition can lead to the generation of new substances that may affect the preparation of perovskite films. Borchert *et al.* reported that perovskite materials begin to decompose above 200 °C and completely decompose at 250 °C.[102] Roß *et al.* investigated the influence of impurities on the evaporation dynamics of MAI.[103] They reported that the thickness of high-purity MAI deposited on QCM after heating was significantly smaller than that of low-purity MAI, making it difficult to effectively monitor the precursor's evaporation rate during vapor deposition of perovskites. Additionally, it is found that the heating process could cause MAI to either decompose or sublime, with the outcome determined by the purity of the MAI. For low-purity MAI, the main pathway was sublimation and deposition on the surface of the QCM (Fig. 8a). For high-purity MAI, most of it decomposed into methylamine (CH_3NH_3I) and hydrogen iodide (HI), after which MAI was regenerated through the reverse reaction (Fig. 8b). However, the decomposition products of MAI were widely distributed in the chamber, and the MAI regenerated through the reverse reaction could not be accurately detected by QCM. This resulted in a significant deviation between the deposited MAI and the added MAI, as evidenced by the different deposition thicknesses of the same mass of MAI on QCM (Fig. 8c). In summary, further research is needed to address the challenges associated with the vapor deposition method, particularly regarding the thermal decomposition of organic compounds

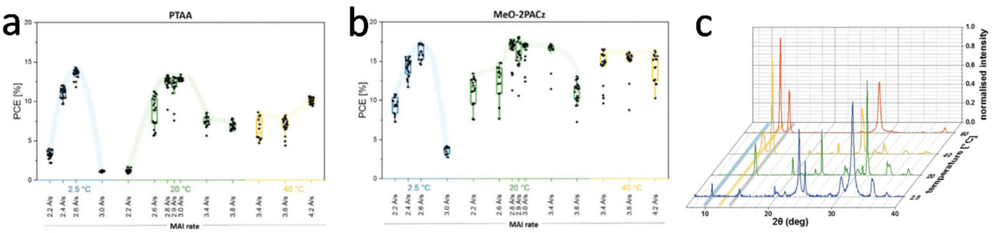

Fig. 7 Box plot of power conversion efficiency extracted from J–V scans (reverse and forward) measured under simulated AM 1.5G illumination for solar cells prepared at different substrate temperatures and MAI rates on (a) PTAA and (b) MeO-2PACz. (c) Normalized XRD patterns of co-evaporated films on PTAA deposited with different substrate temperatures. Reproduced with permission.[101] Copyright 2020, American Chemical Society.

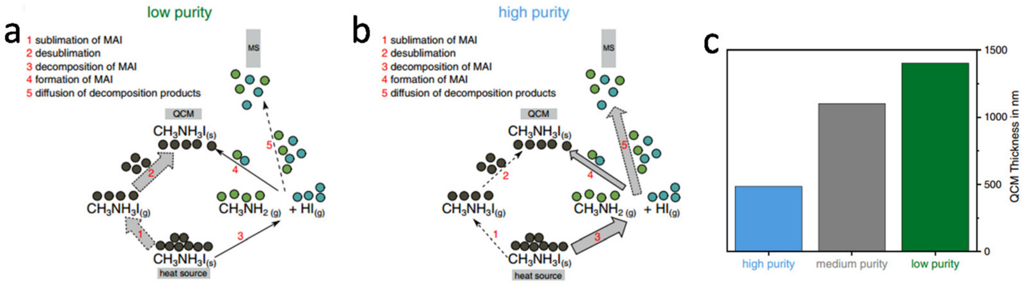

Fig. 8 Schematic of sublimation and decomposition processes. For low purity MAI (a), the main path (thick arrows) is the sublimation and desublimation. For high purity MAI (b), the main path is the decomposition into methylamine and hydrogen iodide. (c) Comparison of the peak areas extracted for each material. Reproduced with permission.[103] Copyright 2022, Wiley-VCH.

within the vacuum chamber. Developing strategies to prevent or control the decomposition of precursors and monitoring their evaporation rates more accurately will be crucial for improving the reproducibility and reliability of the vapor deposition process, ultimately leading to high-quality perovskite films for efficient and stable PSCs.[104]

p-i-n devices in vacuum deposition. The p-i-n perovskite solar cells have advantages such as simple device fabrication, high stability, and negligible hysteresis effect.[105] But their PCEs are still lower than that of n-i-p perovskite solar cells, leaving significant room for improvement and thus are being widely studied. And the PCE gap is more significant in perovskite solar cells prepared by vacuum deposition, which can be attributed to the issue generated from the hole extraction at the "p-i" contact.[106] Poly(3,4-ethylenedioxythiophene)polystyrene sulphonate (PEDOT:PSS) and poly[bis(4-phenyl)(2,4,6-trimethylphenyl)amine] (PTAA) are commonly used HTL materials in PSCs. However, the acidity and hygroscopicity of PEDOT:PSS can lead to decreased stability of PSCs, while the strong hydrophobicity of PTAA results in poor coverage of deposited perovskite films, causing short-circuits in PSCs. Directly vacuum depositing the perovskite on these hydrophobic PTAA layers can be an effective solution to circumvent the coverage issues encountered in solution-based methods.[107] Nevertheless, the selection of hole transport layer (HTL) materials is particularly important, taking into account both electrical connection and manufacturing considerations. The choice of HTL can influence not only the PCE of PSCs but also the optimal conditions for perovskite deposition in terms of substrate temperature and precursor ratio.[101] Thus, it is essential to carefully select and optimize HTL materials that not only enhance the PCE but also ensure compatibility with the chosen perovskite deposition method. Furthermore, the HTL materials should exhibit excellent stability, uniform coverage, and good interface properties with the perovskite layer to reduce recombination losses and improve overall device performance. Recent advances in HTL materials have led to the development of novel alternatives, such as inorganic materials (*e.g.*, triphenylamine-containing pyrrole-based HTM T3) or hybrid organic–inorganic compounds (*e.g.*, Cu:NiO$_x$ with a thin layer of an organic polymer, PhNa-1T), that offer improved stability and interface properties.[108,109] These materials can potentially address the shortcomings of conventional HTL materials like PEDOT:PSS and PTAA, ultimately leading to more efficient and stable PSCs.

Promising potential

Opportunities towards tandem solar cells. The vapor-based deposition method also shows great potential for large-scale fabrication of perovskite films and compatibility with silicon. In 2021, Albrecht *et al.* obtained the first monolithic perovskite/silicon tandem solar cell with an impressive PCE of 24.5% (Fig. 9a).[110] The co-evaporation technique was used to uniformly cover the microscopic pyramidal structure of a typical silicon wafer with $MA_{0.5}FA_{0.63}PbI_{3.13}$. In the wavelength range of 300 to 1200 nm, the PSCs showed significantly lower reflected current losses than planar record tandem solar cells with only 1.62 mA^{-2}.[111] Fig. 9b shows the external quantum

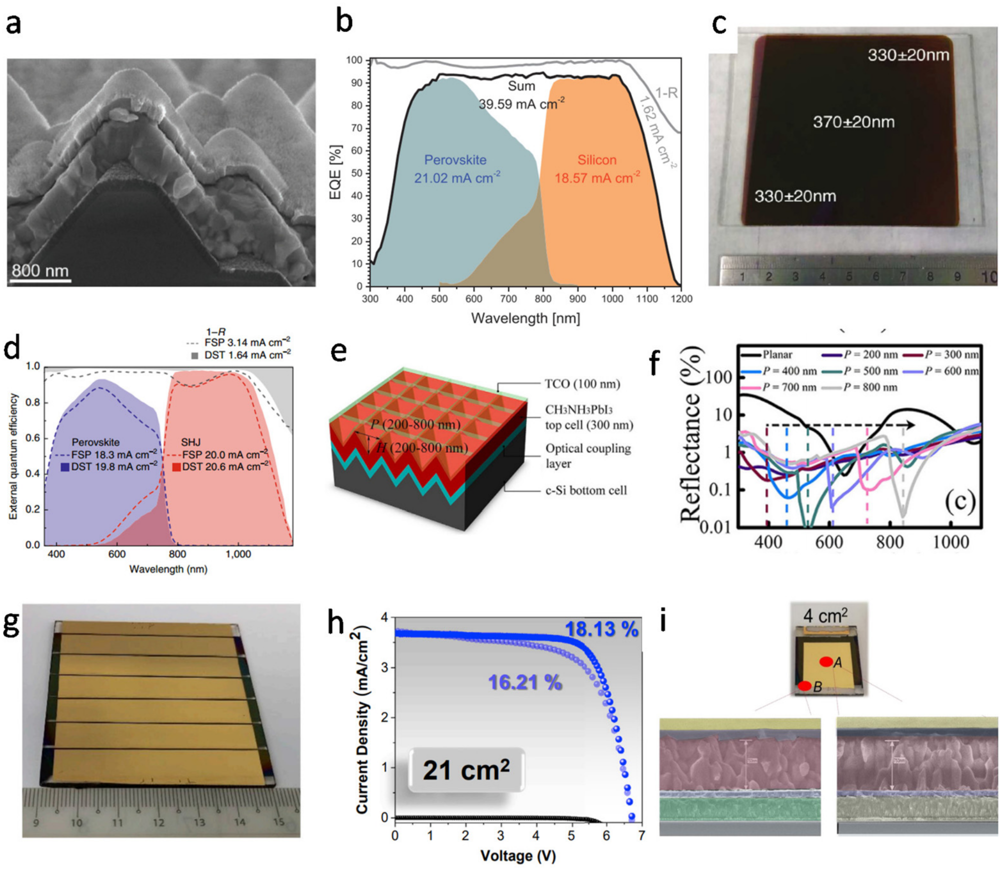

Fig. 9 (a) Cross-sectional SEM image of textured silicon bottom cells covered with $MA_{0.5}FA_{0.63}PbI_{3.13}$, capped with 18 nm of C_{60} and after the 20 nm SnO_2 ALD deposition. Reproduced with permission.[110] Copyright 2021, Wiley-VCH. (b) EQE and reflection spectra (denoted as $1 - R$) including the integrated current densities of the two sub cells, the sum and reflection. Reproduced with permission.[110] Copyright 2021, Wiley-VCH. (c) Photograph of 8 cm × 8 cm thin film of $FAPbI_3$ deposited on a glass substrate. The image shows the substrate after thermal annealing at 170 °C for 1 min. The results of thickness measurements at three positions are superimposed on the image, and a metal ruler with a centimeter scale is shown as a size reference. Reproduced with permission.[116] Copyright 2017, American Chemical Society. (d) Improved optics with a fully textured architecture. EQE of perovskite/SHJ monolithic tandem cells with double-side-textured (DST) or front-side-polished (FSP) bottom cells, alongside corresponding total absorptance curves, $1 - R$, where R is the reflectance of the device. These EQE and $1 - R$ spectra do not include losses due to the front-side metal grid. Reproduced with permission.[113] Copyright 2018, Springer Nature. (e) Schematic of perovskite/c-Si tandem solar cells (TSC) with inverted nanopyramid structure. The parameters H and P denote the pyramid height and its period, respectively. (f) Reflectance of inverted nanopyramid perovskite/c-Si TSC. Reproduced with permission.[115] Copyright 2015, Springer Nature. (g) Image of a 21 cm^2 active area perovskite solar module consisting of 6 series-connected sub-cells. Reproduced with permission.[54] Copyright 2020, Elsevier Inc. (h) Treated-$MAPbI_3$ perovskite solar module dark, forward, and backward J–V curves measured in air. Reproduced with permission.[54] Copyright 2020, Elsevier Inc. (i) 4 cm^2 PSC photograph and cross-sectional SEM images of point A and point B. Reproduced with permission.[54] Copyright 2020, Elsevier Inc.

efficiency (EQE) data and the reflection measurements for the tandem solar cell (denoted as $1 - R$). The pyramid structure on Si has been proved to improve the light absorption and PCE of the perovskite layer.[112–115] Sahli *et al.* demonstrated the advantages of silicon texture by measuring the external quantum efficiency (EQE) of perovskite/silicon heterojunction (SHJ) monolithic tandem cells with double-side-textured (DST) or front-side-polished (FSP) bottom cells.[113] In the perovskite/FSP, the range of reflected light wavelengths was 300 nm to 1200 nm, resulting in a current loss of 3.14 mA cm^{-2}. In contrast, the introduction of front texture in DST led to a reduction in overall reflectance and a decrease in current loss to 1.64 mA cm^{-2} (Fig. 9d). Similar results were observed in the research by Shi *et al.* They reported that silicon cells with pyramid structures exhibited significantly reduced light reflectance for wavelengths between 200 nm to 800 nm compared to flat silicon cells.[115] Furthermore, pyramid structures with different heights and base dimensions were found to have a diminishing effect on light reflectance (Fig. 9e and f). The size of the silicon pyramid texture was found to be strongly correlated with the splitting of quasi-Fermi level (QFLS) and photoluminescence (PL) intensity.[112] As the texture size decreased, PL distribution became more uniform and the distribution of Fermi level was improved. Johnston *et al.* prepared smooth and uniform $FAPbI_3$ films over a large area of about 8 × 8 cm^2, and the PSC fabricated based on the film achieved a stable PCE of 14.2%.[116] Fig. 9c shows the picture of the deposited film after annealing, the thickness of the film substrate center was 370 ± 20 nm, and the thickness at the corners of the substrate dropped to 330 ± 20 nm. These results indicate the possibility of making large-area, homogeneous perovskite films by the evaporation method. In 2020, Bruno *et al.* demonstrated that a PSC mini-module with an active area of 21 cm^2 (Fig. 9g) exhibited a PCE of 18.13% (Fig. 9h).[54] The size of the PSC was scaled up to 4 cm^2 and did not show any significant value loss in V_{oc} and J_{sc} in this large-area PSC, indicating excellent film uniformity (Fig. 9i), confirming the great potential of realizing large-area solar cell architectures through the vapor deposition method.

Low-cost merits. The development of solvent-free synthetic protocols for halide perovskites, such as mechanochemical synthesis and vacuum deposition, offers several advantages over conventional solution processing techniques, resulting in cost reductions and enhanced performance. (a) Reduced material consumption: Mechanochemical synthesis and vacuum deposition methods significantly decrease the usage of precursor materials and solvents. This reduction translates to lower material costs and diminished waste generation during synthesis, contributing to an overall decrease in production expenses. (b) Enhanced material quality: solvent-free synthesis approaches yield higher quality perovskite films with fewer defects, as they circumvent challenges associated with solvent evaporation, residual solvents, and crystallization kinetics commonly encountered in solution-processed films. Consequently, this improvement leads to better performance and stability in perovskite solar cells, culminating in a more cost-effective and dependable product. (c) Streamlined processing and scalability: mechanochemical synthesis and vacuum deposition methods facilitate more straightforward and scalable processing steps, as they eliminate the need for solvents or intricate solution-based procedures. This simplification results in decreased labor and equipment costs and enables easier implementation in large-scale production environments. (d) Augmented environmental sustainability: omitting solvents in these synthesis methods not only reduces the costs related to solvent acquisition and disposal but also minimizes the environmental impact of the manufacturing process. This consideration contributes to a more sustainable and eco-friendly production process, aligning with the growing emphasis on clean energy technologies. (e) Improved compatibility with flexible substrates and tandem solar cells: mechanochemical synthesis and vacuum deposition methods demonstrate better compatibility with flexible substrates and tandem solar cell fabrication, which necessitate precise control over the deposition of multiple layers. The enhanced control and material quality obtained through these methods result in more efficient and cost-effective tandem solar cells, further reducing the overall cost of solar energy production. In conclusion, the transition towards solvent-free synthesis methods, such as mechanochemical synthesis and vacuum deposition, presents substantial cost reductions and performance enhancements for halide perovskite solar cells. These benefits position these methods as a viable alternative to traditional solution processing techniques, supporting the continued advancement of more affordable and efficient solar energy technologies.

Conclusion and perspectives

In conclusion, we have mainly summarized two solvent-free methods for the synthesis of various high-quality perovskites: mechanochemical synthesis and vapor deposition-based synthesis. These two methods can not only circumvent the shortcomings of the mainstream solution-based fabrication methods, such as solvent toxicity, high solvent cost, and poor film formation, but also provide new ideas for the fabrication of large-area perovskite films with excellent optoelectronic properties and greater possibility for mass production considering reproducibility, uniformity, energy–time input, and cleanness, which may pave the route towards real applications based on the halide perovskite materials.

Although the above-mentioned solvent-free synthesis methods are constantly being developed and improved, and significant breakthroughs and achievements have been achieved, there are still problems to be solved and space for improvement. (i) Compared with the solution method, the solvent-free method reduces the toxicity of the solvent, but the involvement of the heavy metal lead in most perovskites still makes the experimental process toxic. While significant progress has been made in the field of Pb-free chalcogenide synthesis,[116] the latest Pb-free PSCs are now available at a maximum of 14.81%. The development of lead-free perovskite with solvent-free synthesis methods would be a landmark solution. (ii) The tunable absorption band gap of perovskite makes it promising for the multi-junction applications. For example, recent studies have demonstrated the preparation of all-perovskite tandem solar cells with record PCE.[117] Briefly, Chiang *et al.* fabricated all-perovskite tandem solar cells using fully-evaporated methods (employing four evaporation sources), which demonstrated an open circuit voltage of 2.06 V and a power conversion efficiency (PCE) of 24.1%.[76] Recognizing this achievement, additional literature on the synthesis of all-perovskite tandem solar cells using vapor-based methods, as opposed to solution-based approaches, also include the following examples. In 2018, Ávila *et al.* demonstrated the preparation of $CH_3NH_3PbI_3$–$CH_3NH_3PbI_3$ tandem solar cells with PCEs exceeding 18%.[117] The devices exhibited a remarkably high open-circuit voltage of 2.3 V, confirming the feasibility of the vapor deposition approach for fabricating high-performance tandem PSCs. In addition to the all-vapor-phase deposition method, researchers have also employed combinations of gas-phase and solution-based approaches for all-perovskite tandem solar cells. Palmstrom *et al.* suggested that an orthogonal solvent system and a solvent-free approach could be utilized to deposit perovskite layers.[118] Furthermore, Abdollahi Nejand *et al.* combined blade coating and vacuum-based deposition processes for the fabrication of all-perovskite tandem solar cells, successfully scaling up laboratory-sized devices from 0.1 cm^2 to 12.25 cm^2.[119] These studies demonstrate the potential of vapor-based and hybrid deposition methods for the fabrication of high-performance all-perovskite tandem solar cells, further validating the relevance and importance of the focus on such approaches. Nevertheless, the perovskite layers in the vast majority of research on all-perovskite tandem solar cells are prepared by solution processing methods, where the presence of solvents has caused many adverse effects on the preparation of high-quality perovskite films as previously discussed. A less or solvent-free synthesis method is expected to optimize the preparation of multi-junction perovskite samples. While the main obstacle is the thickness control in these all-solid methods (for solar cell application the active layer thickness needs to be controlled at the sub-micrometer level to allow sufficient photocarrier drifting), where the mechanochemical methods are less likely compatible but vapor deposition methods hold potential. (iii) The main promise for the mechanochemical methods is the bulk sample application where thermoelectric devices typically require a thick electrode to ensure a sufficient temperature gradient for efficient thermal-electricity conversion, while high energy radiation detectors need a sufficiently large sample thickness to effectively absorb the radiation wave. Although there is a great endeavor being carried out in the direction of perovskite X-ray/gamma-ray detection, most prior reports utilized bulk single crystalline samples for the device. Future works may take advantage of the manufacturing flexibility of the mechanochemical methods to design new p–n junction samples, alloy samples, and multi-layer junction samples for these applications. Further promise can be the development of advanced manufacturing in conjunction with 3D printing techniques, mold printing, laser annealing, *etc*.

Conflicts of interest

There are no conflicts to declare.

Acknowledgements

The authors from NPU acknowledge financial support from the Fundamental Research Funds for the Central Universities (D5000220072). The unfunded collaborative work of L. Z., A. N., B. P., and K. W. is supported by the International Institute of Biosensing (IIB), headquartered at Penn State University.

References

1 P. Pal, S. Saha, A. Banik, A. Sarkar and K. Biswas, All-Solid-State Mechanochemical Synthesis and Post-Synthetic Transformation of Inorganic Perovskite-type Halides, *Chem. – Eur. J.*, 2018, **24**, 1811–1815.

2 K. Wang, D. Yang, C. Wu, M. Sanghadasa and S. Priya, Recent progress in fundamental understanding of halide perovskite semiconductors, *Prog. Mater. Sci.*, 2019, **106**, 100580.

3 R. Vidal, J.-A. Alberola-Borràs, S. N. Habisreutinger, J.-L. Gimeno-Molina, D. T. Moore, T. H. Schloemer, I. Mora-Seró, J. J. Berry and J. M. Luther, Assessing health and environmental impacts of solvents for producing perovskite solar cells, *Nat. Sustainability*, 2021, **4**, 277–285.

4 L. Zheng, A. Nozariasbmarz, Y. Hou, J. Yoon, W. Li, Y. Zhang, H. Wu, D. Yang, T. Ye, M. Sanghadasa, K. Wang, B. Poudel, S. Priya and K. Wang, A universal all-solid synthesis for high throughput production of halide perovskite, *Nat. Commun.*, 2022, **13**, 7399.

5 G. Cao, *Nanostructures & nanomaterials: synthesis, properties & applications*, Imperial College Press, 2004.

6 B. Ding, Y. Li, S.-Y. Huang, Q.-Q. Chu, C.-X. Li, C.-J. Li and G.-J. Yang, Material nucleation/growth competition tuning towards highly reproducible planar perovskite solar cells with efficiency exceeding 20%, *J. Mater. Chem. A*, 2017, **5**, 6840–6848.

7 M. Haruta and B. Delmon, Preparation of homodisperse solids, *J. Chim. Phys.*, 1986, **83**, 859–868.

8 Y. Fu, F. Meng, M. B. Rowley, B. J. Thompson, M. J. Shearer, D. Ma, R. J. Hamers, J. C. Wright and S. Jin, Solution growth of single crystal methylammonium lead halide perovskite nanostructures for optoelectronic and photovoltaic applications, *J. Am. Chem. Soc.*, 2015, **137**, 5810–5818.

9 F. Huang, M. Li, P. Siffalovic, G. Cao and J. Tian, From scalable solution fabrication of perovskite films towards commercialization of solar cells, *Energy Environ. Sci.*, 2019, **12**, 518–549.

10 S. J. Yoon, K. G. Stamplecoskie and P. V. Kamat, How lead halide complex chemistry dictates the composition of mixed halide perovskites, *J. Phys. Chem. Lett.*, 2016, **7**, 1368–1373.

11 B. A. Rosales, L. Men, S. D. Cady, M. P. Hanrahan, A. J. Rossini and J. Vela, Persistent dopants and phase segregation in organolead mixed-halide perovskites, *Chem. Mater.*, 2016, **28**, 6848–6859.

12 B. A. Rosales, M. P. Hanrahan, B. W. Boote, A. J. Rossini, E. A. Smith and J. Vela, Lead halide perovskites: Challenges and opportunities in advanced synthesis and spectroscopy, *ACS Energy Lett.*, 2017, **2**, 906–914.

13 L. Men, M. A. White, H. Andaraarachchi, B. A. Rosales and J. Vela, Synthetic development of low dimensional materials, *Chem. Mater.*, 2017, **29**, 168–175.

14 A. Karmakar, A. M. Askar, G. M. Bernard, V. V. Terskikh, M. Ha, S. Patel, K. Shankar and V. K. Michaelis, Mechanochemical synthesis of methylammonium lead mixed–halide perovskites: unraveling the solid-solution behavior using solid-state NMR, *Chem. Mater.*, 2018, **30**, 2309–2321.

15 M. P. Hanrahan, L. Men, B. A. Rosales, J. Vela and A. J. Rossini, Sensitivity-enhanced ^{207}Pb solid-state NMR spectroscopy for the rapid, non-destructive characterization of organolead halide perovskites, *Chem. Mater.*, 2018, **30**, 7005–7015.

16 F. Brivio, C. Caetano and A. Walsh, Thermodynamic origin of photoinstability in the $CH_3NH_3Pb(I_{1-x}Br_x)_3$ hybrid halide perovskite alloy, *J. Phys. Chem. Lett.*, 2016, **7**, 1083–1087.

17 A. M. Askar, A. Karmakar, G. M. Bernard, M. Ha, V. V. Terskikh, B. D. Wiltshire, S. Patel, J. Fleet, K. Shankar and V. K. Michaelis, Composition-tunable formamidinium lead mixed halide perovskites via solvent-free mechanochemical synthesis: decoding the Pb environments using solid-state NMR spectroscopy, *J. Phys. Chem. Lett.*, 2018, **9**, 2671–2677.

18 N. K. Noel, S. N. Habisreutinger, B. Wenger, M. T. Klug, M. T. Hörantner, M. B. Johnston, R. J. Nicholas, D. T. Moore and H. J. Snaith, A low viscosity, low boiling point, clean solvent system for the rapid crystallisation of highly specular perovskite films, *Energy Environ. Sci.*, 2017, **10**, 145–152.

19 X. Cao, L. Zhi, Y. Jia, Y. Li, K. Zhao, X. Cui, L. Ci, D. Zhuang and J. Wei, A review of the role of solvents in formation of high-quality solution-processed perovskite films, *ACS Appl. Mater. Interfaces*, 2019, **11**, 7639–7654.

20 J. Schlipf, P. Docampo, C. J. Schaffer, V. Körstgens, L. Bießmann, F. Hanusch, N. Giesbrecht, S. Bernstorff, T. Bein and P. Müller-Buschbaum, A closer look into two-step perovskite conversion with X-ray scattering, *J. Phys. Chem. Lett.*, 2015, **6**, 1265–1269.

21 R. Liu and K. J. M. Xu, Solvent engineering for perovskite solar cells: a review, *Micro Nano Lett.*, 2020, **15**, 349–353.

22 Y.-H. Seo, E.-C. Kim, S.-P. Cho, S.-S. Kim and S.-I. Na, High-performance planar perovskite solar cells: Influence of solvent upon performance, *Appl. Mater. Today*, 2017, **9**, 598–604.

23 Y. Li, Z. Zhao, F. Lin, X. Cao, X. Cui and J. Wei, In situ observation of crystallization of methylammonium lead iodide perovskite from microdroplets, *Small*, 2017, **13**, 1604125.

24 B. Cai, W.-H. Zhang and J. Qiu, Solvent engineering of spin-coating solutions for planar-structured high-efficiency perovskite solar cells, *Chin. J. Catal.*, 2015, **36**, 1183–1190.

25 N. Ahn, D.-Y. Son, I.-H. Jang, S. M. Kang, M. Choi and N.-G. Park, Highly reproducible perovskite solar cells with average efficiency of 18.3% and best efficiency of 19.7% fabricated via Lewis base adduct of lead(II) iodide, *J. Am. Chem. Soc.*, 2015, **137**, 8696–8699.

26 J. Zhao, Y. Deng, H. Wei, X. Zheng, Z. Yu, Y. Shao, J. E. Shield and J. Huang, Strained hybrid perovskite thin films and their impact on the intrinsic stability of perovskite solar cells, *Sci. Adv.*, 2017, **3**, 5616.

27 C. N. R. Rao and K. Biswas, Soft Chemistry Routes, *Essentials of Inorganic Materials Synthesis*, 2015.

28 H. Zhou, Q. Chen, G. Li, S. Luo, T.-B. Song, H.-S. Duan, Z. Hong, J. You, Y. Liu and Y. Yang, Interface engineering of highly efficient perovskite solar cells, *Science*, 2014, **345**, 542–546.

29 R. Karlicek, C.-C. Sun, G. Zissis and R. Ma, *Handbook of advanced lighting technology*, Springer, 2017.

30 X. Cao, L. Zhi, Y. Li, F. Fang, X. Cui, L. Ci, K. Ding and J. Wei, Fabrication of perovskite films with large columnar grains via solvent-mediated Ostwald ripening for efficient inverted perovskite solar cells, *ACS Appl. Energy Mater.*, 2018, **1**, 868–875.

31 J.-H. Im, I.-H. Jang, N. Pellet, M. Grätzel and N.-G. Park, Growth of $CH_3NH_3PbI_3$ cuboids with controlled size for high-efficiency perovskite solar cells, *Nat. Nanotechnol.*, 2014, **9**, 927–932.

32 J. H. Heo, F. Zhang, C. Xiao, S. J. Heo, J. K. Park, J. J. Berry, K. Zhu and S. H. Im, Efficient and stable graded $CsPbI_{3-x}Br_x$ perovskite solar cells and submodules by orthogonal processable spray coating, *Joule*, 2021, **5**, 481–494.

33 X. Jia, C. Zuo, S. Tao, K. Sun, Y. Zhao, S. Yang, M. Cheng, M. Wang, Y. Yuan and J. Yang, $CsPb(I_xBr_{1-x})_3$ solar cells, *Sci. Bull. Fac. Agric., Kyushu Univ.*, 2019, **64**, 1532–1539.

34 Y. Wang, T. Zhang, M. Kan, Y. Li, T. Wang and Y. Zhao, Efficient α-$CsPbI_3$ photovoltaics with surface terminated organic cations, *Joule*, 2018, **2**, 2065–2075.

35 M. Tai, Y. Zhou, X. Yin, J. Han, Q. Zhang, Y. Zhou and H. Lin, In situ formation of a 2D/3D heterostructure for efficient and stable $CsPbI_2$ Br solar cells, *J. Mater. Chem. A*, 2019, **7**, 22675–22682.

36 L. Protesescu, S. Yakunin, O. Nazarenko, D. N. Dirin and M. V. Kovalenko, Low-cost synthesis of highly luminescent colloidal lead halide perovskite nanocrystals by wet ball milling, *ACS Appl. Nano Mater.*, 2018, **1**, 1300–1308.

37 P. Sebastia-Luna, J. Navarro-Alapont, M. Sessolo, F. Palazon and H. J. Bolink, Solvent-free synthesis and thin-film deposition of cesium copper halides with bright blue photoluminescence, *Chem. Mater.*, 2019, **31**, 10205–10210.

38 V. M. Kiyek, Y. A. Birkhölzer, Y. Smirnov, M. Ledinsky, Z. Remes, J. Momand, B. J. Kooi, G. Koster, G. Rijnders and M. Morales-Masis, Single-source, solvent-free, room temperature deposition of black γ-$CsSnI_3$ films, *Adv. Mater. Interfaces*, 2020, **7**, 2000162.

39 E. M. Gutman, *Mechanochemistry of materials*, Cambridge Int Science Publishing, 1998.

40 B. A. Rosales, L. Wei and J. Vela, Synthesis and mixing of complex halide perovskites by solvent-free solid-state methods, *J. Solid State Chem.*, 2019, **271**, 206–215.

41 O. Y. Posudievsky, N. V. Konoshchuk, A. G. Shkavro, V. L. Karbivskiy, V. G. Koshechko and V. D. Pokhodenko, Nanostructured Mechanochemically Prepared Hybrid Perovskites Based on PbI_2 and Alkylammonium Halides for Optoelectronic Applications, *ACS Appl. Nano Mater.*, 2018, **1**, 4145–4155.

42 B. A. Huisman, F. Palazon and H. J. Bolink, Zero-dimensional hybrid organic–inorganic lead halides and their post-synthesis reversible transformation into three-dimensional perovskites, *Inorg. Chem.*, 2021, **60**, 5212–5216.

43 M. Era, T. Hattori, T. Taira and T. Tsutsui, Self-organized growth of PbI-based layered perovskite quantum well by dual-source vapor deposition, *Chem. Mater.*, 1997, **9**, 8–10.

44 M. Liu, M. B. Johnston and H. J. Snaith, Efficient planar heterojunction perovskite solar cells by vapour deposition, *Nature*, 2013, **501**, 395–398.

45 H. Li, J. Zhou, L. Tan, M. Li, C. Jiang, S. Wang, X. Zhao, Y. Liu, Y. Zhang, Y. Ye, W. Tress and C. Yi, Sequential vacuum-evaporated perovskite solar cells with more than 24% efficiency, *Sci. Adv.*, 2022, **8**, 7422.

46 C. W. Chen, H. W. Kang, S. Y. Hsiao, P. F. Yang, K. M. Chiang and H. W. Lin, Efficient and uniform planar-type perovskite solar cells by simple sequential vacuum deposition, *Adv. Mater.*, 2014, **26**, 6647–6652.

47 L. K. Ono, S. Wang, Y. Kato, S. R. Raga and Y. Qi, Fabrication of semi-transparent perovskite films with centimeter-scale superior uniformity by the hybrid deposition method, *Energy Environ. Sci.*, 2014, **7**, 3989–3993.

48 D. Yang, Z. Yang, W. Qin, Y. Zhang, S. F. Liu and C. Li, Alternating precursor layer deposition for highly stable perovskite films towards efficient solar cells using vacuum deposition, *J. Mater. Chem. A*, 2015, **3**, 9401–9405.

49 G. Longo, C. Momblona, M.-G. La-Placa, L. N. Gil-Escrig, M. Sessolo and H. J. Bolink, Fully vacuum-processed wide band gap mixed-halide perovskite solar cells, *ACS Energy Lett.*, 2018, **3**, 214–219.

50 M. Kam, Y. Zhu, D. Zhang, L. Gu, J. Chen and Z. Fan, Efficient mixed-cation mixed-halide perovskite solar cells by all-vacuum sequential deposition using metal oxide electron transport layer, *Sol. RRL*, 2019, **3**, 1900050.

51 K. B. Lohmann, J. B. Patel, M. U. Rothmann, C. Q. Xia, R. D. Oliver, L. M. Herz, H. J. Snaith and M. B. Johnston, Control over crystal size in vapor deposited metal–halide perovskite films, *ACS Energy Lett.*, 2020, **5**, 710–717.

52 J. B. Patel, Q. Lin, O. Zadvorna, C. L. Davies, L. M. Herz and M. B. Johnston, Photocurrent spectroscopy of perovskite solar cells over a wide temperature range from 15 to 350 K, *J. Phys. Chem. Lett.*, 2018, **9**, 263–268.

53 F. Liu, Q. Dong, M. K. Wong, A. B. Djurišić, A. Ng, Z. Ren, Q. Shen, C. Surya, W. K. Chan and J. Wang, Is excess PbI_2 beneficial for perovskite solar cell performance?, *Adv. Energy Mater.*, 2016, **6**, 1502206.

54 J. Li, H. Wang, X. Y. Chin, H. A. Dewi, K. Vergeer, T. W. Goh, J. W. M. Lim, J. H. Lew, K. P. Loh, C. Soci, T. C. Sum, H. J. Bolink, N. Mathews, S. Mhaisalkar and A. Bruno, Highly efficient thermally co-evaporated perovskite solar cells and mini-modules, *Joule*, 2020, **4**, 1035–1053.

55 B. Chen, P. N. Rudd, S. Yang, Y. Yuan and J. Huang, Imperfections and their passivation in halide perovskite solar cells, *Chem. Soc. Rev.*, 2019, **48**, 3842–3867.

56 J. Feng, Y. Jiao, H. Wang, X. Zhu, Y. Sun, M. Du, Y. Cao, D. Yang and S. F. Liu, High-throughput large-area vacuum deposition for high-performance formamidine-based perovskite solar cells, *Energy Environ. Sci.*, 2021, **14**, 3035–3043.

57 B. Conings, J. Drijkoningen, N. Gauquelin, A. Babayigit, J. D'Haen, L. D'Olieslaeger, A. Ethirajan, J. Verbeeck, J. Manca and E. Mosconi, Intrinsic thermal instability of methylammonium lead trihalide perovskite, *Adv. Energy Mater.*, 2015, **5**, 1500477.

58 C. Quarti, E. Mosconi, J. M. Ball, V. D'Innocenzo, C. Tao, S. Pathak, H. J. Snaith, A. Petrozza and F. De Angelis, Structural and optical properties of methylammonium lead iodide across the tetragonal to cubic phase transition: implications for perovskite solar cells, *Energy Environ. Sci.*, 2016, **9**, 155–163.

59 E. J. Juarez-Perez, Z. Hawash, S. R. Raga, L. K. Ono and Y. Qi, Thermal degradation of $CH_3NH_3PbI_3$ perovskite into NH_3 and CH_3I gases observed by coupled thermogravimetry–mass spectrometry analysis, *Energy Environ. Sci.*, 2016, **9**, 3406–3410.

60 J. J. Yoo, G. Seo, M. R. Chua, T. G. Park, Y. Lu, F. Rotermund, Y.-K. Kim, C. S. Moon, N. J. Jeon and J.-P. Correa-Baena, Efficient perovskite solar cells via improved carrier management, *Nature*, 2021, **590**, 587–593.

61 M. Kim, G.-H. Kim, T. K. Lee, I. W. Choi, H. W. Choi, Y. Jo, Y. J. Yoon, J. W. Kim, J. Lee and D. Huh, Methylammonium chloride induces intermediate phase stabilization for efficient perovskite solar cells, *Joule*, 2019, **3**, 2179–2192.

62 W. Shockley and H. J. Queisser, Detailed balance limit of efficiency of p–n junction solar cells, *J. Appl. Phys.*, 1961, **32**, 510–519.

63 Q. Jiang, Y. Zhao, X. Zhang, X. Yang, Y. Chen, Z. Chu, Q. Ye, X. Li, Z. Yin and J. You, Surface passivation of perovskite film for efficient solar cells, *Nat. Photonics*, 2019, **13**, 460–466.

64 S.-H. Turren-Cruz, A. Hagfeldt and M. Saliba, Methylammonium-free, high-performance, and stable perovskite solar cells on a planar architecture, *Science*, 2018, **362**, 449–453.

65 G. E. Eperon, S. D. Stranks, C. Menelaou, M. B. Johnston, L. M. Herz and H. J. Snaith, Formamidinium lead trihalide: a broadly tunable perovskite for efficient planar heterojunction solar cells, *Energy Environ. Sci.*, 2014, **7**, 982–988.

66 J. W. Lee, D. H. Kim, H. S. Kim, S. W. Seo, S. M. Cho and N. G. Park, Formamidinium and cesium hybridization for photo- and moisture-stable perovskite solar cell, *Adv. Energy Mater.*, 2015, **5**, 1501310.

67 C. Yi, J. Luo, S. Meloni, A. Boziki, N. Ashari-Astani, C. Grätzel, S. M. Zakeeruddin, U. Röthlisberger and M. Grätzel, Entropic stabilization of mixed A-cation ABX_3 metal halide perovskites for high performance perovskite solar cells, *Energy Environ. Sci.*, 2016, **9**, 656–662.

68 Z. Li, M. Yang, J.-S. Park, S.-H. Wei, J. J. Berry and K. Zhu, Stabilizing perovskite structures by tuning tolerance factor: formation of formamidinium and cesium lead iodide solid-state alloys, *Chem. Mater.*, 2016, **28**, 284–292.

69 W. Qiu, A. Ray, M. Jaysankar, T. Merckx, J. P. Bastos, D. Cheyns, R. Gehlhaar, J. Poortmans and P. Heremans, An interdiffusion method for highly performing cesium/formamidinium double cation perovskites, *Adv. Funct. Mater.*, 2017, **27**, 1700920.

70 K. Schutt, P. K. Nayak, A. J. Ramadan, B. Wenger, Y. H. Lin and H. J. Snaith, Overcoming zinc oxide interface instability with a methylammonium-free perovskite for high-performance solar cells, *Adv. Funct. Mater.*, 2019, **29**, 1900466.

71 S. Chen, L. Pan, T. Ye, N. Lei, Y. Yang and X. Wang, The lattice reconstruction of Cs-introduced $FAPbI_{1.80}Br_{1.20}$ enables improved stability for perovskite solar cells, *RSC Adv.*, 2021, **11**, 3997–4005.

72 T. Ye, S.-L. Lim, X. Li, M. Petrović, X. Wang, C. Jiang, W.-P. Goh, C. Vijila and S. Ramakrishna, Pinhole-free-mixed perovskite film for bending durable mixed perovskite solar cells, *Sol. Energy Mater. Sol. Cells*, 2018, **175**, 111–117.

73 X. Zhu, D. Yang, R. Yang, B. Yang, Z. Yang, X. Ren, J. Zhang, J. Niu, J. Feng and S. F. Liu, Superior stability for perovskite solar cells with 20% efficiency using vacuum co-evaporation, *Nanoscale*, 2017, **9**, 12316–12323.

74 M. Saliba, T. Matsui, J.-Y. Seo, K. Domanski, J.-P. Correa-Baena, M. K. Nazeeruddin, S. M. Zakeeruddin, W. Tress, A. Abate and A. Hagfeldt, Cesium-containing triple cation perovskite solar cells: improved stability, reproducibility and high efficiency, *Energy Environ. Sci.*, 2016, **9**, 1989–1997.

75 L. Gil-Escrig, C. Momblona, M. G. La-Placa, P. P. Boix, M. Sessolo and H. J. Bolink, Vacuum deposited triple-cation mixed-halide perovskite solar cells, *Adv. Energy Mater.*, 2018, **8**, 1703506.

76 Y.-H. Chiang, M. Anaya and S. D. Stranks, Multisource vacuum deposition of methylammonium-free perovskite solar cells, *ACS Energy Lett.*, 2020, **5**, 2498–2504.

77 X. Deng, J. Hua, F. Huang, Y. Peng, W. Li, Z. Ku and Y.-B. Cheng, Improving the crystal growth of a $Cs_{0.24}FA_{0.76}PbI_{3-x}Br_x$ perovskite in a vapor–solid reaction process using strontium iodide, *Sustainable Energy Fuels*, 2020, **4**, 2491–2496.

78 L. Gil-Escrig, C. Dreessen, F. Palazon, Z. Hawash, E. Moons, S. Albrecht, M. Sessolo and H. J. Bolink, Efficient wide-bandgap mixed-cation and mixed-halide perovskite solar cells by vacuum deposition, *ACS Energy Lett.*, 2021, **6**, 827–836.

79 L. Zhao, Y. Gao, M. Su, Q. Shang, Z. Liu, Q. Li, Q. Wei, M. Li, L. Fu and Y. Zhong, Vapor-phase incommensurate heteroepitaxy of oriented single-crystal $CsPbBr_3$ on GaN: toward integrated optoelectronic applications, *ACS Nano*, 2019, **13**, 10085–10094.

80 Y. Zhou, K. Fernando, J. Wan, F. Liu, S. Shrestha, J. Tisdale, C. J. Sheehan, A. C. Jones, S. Tretiak and H. Tsai, Millimeter-size all-inorganic perovskite crystalline thin film grown by chemical vapor deposition, *Adv. Funct. Mater.*, 2021, **31**, 2101058.

81 J. Chen, D. J. Morrow, Y. Fu, W. Zheng, Y. Zhao, L. Dang, M. J. Stolt, D. D. Kohler, X. Wang and K. J. Czech, Single-crystal thin films of cesium lead bromide perovskite epitaxially grown on metal oxide perovskite ($SrTiO_3$), *J. Am. Chem. Soc.*, 2017, **139**, 13525–13532.

82 F. Gao, Y. Zhao, X. Zhang and J. You, Recent progresses on defect passivation toward efficient perovskite solar cells, *Adv. Energy Mater.*, 2020, **10**, 1902650.

83 Y. Fan, H. Meng, L. Wang and S. Pang, Review of stability enhancement for formamidinium-based perovskites, *Sol. RRL*, 2019, **3**, 1900215.

84 M. Lyu and N.-G. Park, Effect of additives AX (A = FA, MA, Cs, Rb, NH_4, X = Cl, Br, I) in $FAPbI_3$ on photovoltaic parameters of perovskite solar cells, *Sol. RRL*, 2020, **4**, 2000331.

85 J.-W. Lee, Z. Dai, C. Lee, H. M. Lee, T.-H. Han, N. De Marco, O. Lin, C. S. Choi, B. Dunn and J. Koh, Tuning molecular interactions for highly reproducible and efficient formamidinium perovskite solar cells via adduct approach, *J. Am. Chem. Soc.*, 2018, **140**, 6317–6324.

86 R. Kennedy, R. Madden and P. Stampe, Effects of substrate temperature on the growth and properties of $SrRuO_3$ and $CaRuO_3$ thin films, *J. Phys. D: Appl. Phys.*, 2001, **34**, 1853.

87 A. R. Patel and D. Lakshminarayana, Effect of substrate temperature on the crystallinity of $AgSbSe_2$ films, *Thin Solid Films*, 1982, **98**, 59–63.

88 B. Borer, A. Sonnenfeld and P. R. von Rohr, Influence of substrate temperature on morphology of SiOx films deposited on particles by PECVD, *Surf. Coat. Technol.*, 2006, **201**, 1757–1762.

89 S. Wang, L. K. Ono, M. R. Leyden, Y. Kato, S. R. Raga, M. V. Lee and Y. Qi, Smooth perovskite thin films and efficient perovskite solar cells prepared by the hybrid deposition method, *J. Mater. Chem. A*, 2015, **3**, 14631–14641.

90 J. Ávila, C. Momblona, P. P. Boix, M. Sessolo and H. J. Bolink, Vapor-deposited perovskites: the route to high-performance solar cell production?, *Joule*, 2017, **1**, 431–442.

91 X. Zhou, X. Li, Y. Liu, F. Huang and D. Zhong, Interface electronic properties of co-evaporated $MAPbI_3$ on ZnO (0001): In situ X-ray photoelectron spectroscopy and ultraviolet photoelectron spectroscopy study, *Appl. Phys. Lett.*, 2016, **108**, 121601.

92 H. Xu, Y. Wu, J. Cui, C. Ni, F. Xu, J. Cai, F. Hong, Z. Fang, W. Wang and J. Zhu, Formation and evolution of the unexpected PbI_2 phase at the interface during the growth of evaporated perovskite films, *Phys. Chem. Chem. Phys.*, 2016, **18**, 18607–18613.

93 T. Ye, G. Han, A. Surendran, J. Li, T. M. Koh, S. G. Mhaisalkar and W. L. Leong, Large area, high efficiency and stable perovskite solar cells enabled by fine control of intermediate phase, *Sol. Energy Mater. Sol. Cells*, 2019, **201**, 110113.

94 K. X. Steirer, P. Schulz, G. Teeter, V. Stevanovic, M. Yang, K. Zhu and J. J. Berry, Defect tolerance in methylammonium lead triiodide perovskite, *ACS Energy Lett.*, 2016, **1**, 360–366.

95 J. W. Lee, D. K. Lee, D. N. Jeong and N. G. Park, Control of crystal growth toward scalable fabrication of perovskite solar cells, *Adv. Funct. Mater.*, 2019, **29**, 1807047.

96 X. Wang, Y. Fan, L. Wang, C. Chen, Z. Li, R. Liu, H. Meng, Z. Shao, X. Du and H. Zhang, Perovskite solution aging: what happened and how to inhibit?, *Chem*, 2020, **6**, 1369–1378.

97 H. Min, G. Kim, M. J. Paik, S. Lee, W. S. Yang, M. Jung and S. I. Seok, Stabilization of precursor solution and perovskite layer by addition of sulfur, *Adv. Energy Mater.*, 2019, **9**, 1803476.

98 G. S. Shin, Y. Zhang and N.-G. Park, Stability of precursor solution for perovskite solar cell: Mixture (FAI + PbI_2) versus synthetic $FAPbI_3$ crystal, *ACS Appl. Mater. Interfaces*, 2020, **12**, 15167–15174.

99 J. H. Lee, B. S. Kim, J. Park, J. W. Lee and K. Kim, Opportunities and challenges for perovskite solar cells based on vacuum thermal evaporation, *Adv. Mater. Technol.*, 2022, 2200928.

100 B.-S. Kim, L. Gil-Escrig, M. Sessolo and H. J. Bolink, Deposition kinetics and compositional control of vacuum-processed $CH_3NH_3PbI_3$ perovskite, *J. Phys. Chem. Lett.*, 2020, **11**, 6852–6859.

101 M. Roß, L. Gil-Escrig, A. Al-Ashouri, P. Tockhorn, M. Jost, B. Rech and S. Albrecht, Co-evaporated p-i-n perovskite solar cells beyond 20% efficiency: impact of substrate temperature and hole-transport layer, *ACS Appl. Mater. Interfaces*, 2020, **12**, 39261–39272.

102 J. Borchert, H. Boht, W. Fränzel, R. Csuk, R. Scheer and P. Pistor, Structural investigation of co-evaporated methyl ammonium lead halide perovskite films during growth and thermal decomposition using different PbX_2 (X = I, Cl) precursors, *J. Mater. Chem. A*, 2015, **3**, 19842–19849.

103 M. Roß, M. B. Stutz and S. Albrecht, Revealing the Role of Methylammonium Iodide Purity on the Vapor-Phase Deposition Process of Perovskites, *Sol. RRL*, 2022, **6**, 2200500.

104 J. Borchert, I. Levchuk, L. C. Snoek, M. U. Rothmann, R. E. Haver, H. J. Snaith, C. J. Brabec, L. M. Herz and M. B. Johnston, Impurity tracking enables enhanced control and reproducibility of hybrid perovskite vapor deposition, *ACS Appl. Mater. Interfaces*, 2019, **11**, 28851–28857.

105 T. Liu, K. Chen, Q. Hu, R. Zhu and Q. Gong, Inverted perovskite solar cells: progresses and perspectives, *Adv. Energy Mater.*, 2016, **6**, 1600457.

106 C. Momblona, L. Gil-Escrig, E. Bandiello, E. M. Hutter, M. Sessolo, K. Lederer, J. Blochwitz-Nimoth and H. J. Bolink, Efficient vacuum deposited p-i-n and n-i-p perovskite solar cells employing doped charge transport layers, *Energy Environ. Sci.*, 2016, **9**, 3456–3463.

107 S. S. Mali and C. K. Hong, p-i-n/n-i-p type planar hybrid structure of highly efficient perovskite solar cells towards improved air stability: synthetic strategies and the role of p-type hole transport layer (HTL) and n-type electron transport layer (ETL) metal oxides, *Nanoscale*, 2016, **8**, 10528–10540.

108 J. Zhou, H. Li, L. Tan, Y. Liu, J. Yang, R. Hua and C. Yi, Tuning Hole Transport Properties via Pyrrole Derivation for High-Performance Perovskite Solar Cells, *Angew. Chem., Int. Ed.*, 2023, **62**, e202300314.

109 J. W. Jo, M.-S. Seo, J. W. Jung, J.-S. Park, B.-H. Sohn, M. J. Ko and H. J. Son, Development of organic-inorganic double hole-transporting material for high performance perovskite solar cells, *J. Power Sources*, 2018, **378**, 98–104.

110 M. Roß, S. Severin, M. B. Stutz, P. Wagner, H. Köbler, M. Favin-Lévêque, A. Al-Ashouri, P. Korb, P. Tockhorn, A. Abate, B. Stannowski, B. Rech and S. Albrecht, Co-Evaporated Formamidinium Lead Iodide Based Perovskites with 1000 h Constant Stability for Fully Textured Monolithic Perovskite/Silicon Tandem Solar Cells, *Adv. Energy Mater.*, 2021, **11**, 2101460.

111 A. Al-Ashouri, E. Köhnen, B. Li, A. Magomedov, H. Hempel, P. Caprioglio, J. A. Márquez, A. B. Morales Vilches, E. Kasparavicius and J. A. Smith, Monolithic perovskite/silicon tandem solar cell with >29% efficiency by enhanced hole extraction, *Science*, 2020, **370**, 1300–1309.

112 E. M. Tennyson, K. Frohna, W. K. Drake, F. Sahli, T. Chien-Jen Yang, F. Fu, J. Werner, C. Chosy, A. R. Bowman and T. A. Doherty, Multimodal microscale imaging of textured perovskite–silicon tandem solar cells, *ACS Energy Lett.*, 2021, **6**, 2293–2304.

113 F. Sahli, J. Werner, B. A. Kamino, M. Bräuninger, R. Monnard, B. Paviet-Salomon, L. Barraud, L. Ding, J. J. Diaz Leon, D. Sacchetto, *et al.*, Fully textured monolithic perovskite/silicon tandem solar cells with 25.2% power conversion efficiency, *Nat. Mater.*, 2018, **17**, 820–826.

114 L. Duan, D. Walter, N. Chang, J. Bullock, D. Kang, S. P. Phang, K. Weber, T. White, D. Macdonald, K. Catchpole and H. Shen, Stability challenges for the commercialization of perovskite–silicon tandem solar cells, *Nat. Rev. Mater.*, 2023, **8**, 261–281.

115 D. Shi, Y. Zeng and W. Shen, Perovskite/c-Si tandem solar cell with inverted nanopyramids: realizing high efficiency by controllable light trapping, *Sci. Rep.*, 2015, **5**, 16504.

116 J. Borchert, R. L. Milot, J. B. Patel, C. L. Davies, A. D. Wright, L. Martínez Maestro, H. J. Snaith, L. M. Herz and M. B. Johnston, Large-area, highly uniform evaporated formamidinium lead triiodide thin films for solar cells, *ACS Energy Lett.*, 2017, **2**, 2799–2804.

117 J. Ávila, C. Momblona, P. Boix, M. Sessolo, M. Anaya, G. Lozano, K. Vandewal, H. Míguez and H. J. Bolink, High voltage vacuum-deposited $CH_3NH_3PbI_3$–$CH_3NH_3PbI_3$ tandem solar cells, *Energy Environ. Sci.*, 2018, **11**, 3292–3297.

118 A. F. Palmstrom, G. E. Eperon, T. Leijtens, R. Prasanna, S. N. Habisreutinger, W. Nemeth, E. A. Gaulding, S. P. Dunfield, M. Reese and S. Nanayakkara, Enabling flexible all-perovskite tandem solar cells, *Joule*, 2019, **3**, 2193–2204.

119 B. Abdollahi Nejand, D. B. Ritzer, H. Hu, F. Schackmar, S. Moghadamzadeh, T. Feeney, R. Singh, F. Laufer, R. Schmager and R. Azmi, Scalable two-terminal all-perovskite tandem solar modules with a 19.1% efficiency, *Nat. Energy*, 2022, **7**, 620–630.